INORGANIC CHEMISTRY
FRONTIERS

REVIEW

View Article Online
View Journal | View Issue

Check for updates

Cite this: *Inorg. Chem. Front.*, 2023, **10**, 3489

# Recent progress and strategies on the design of catalysts for electrochemical ammonia synthesis from nitrate reduction

Wei Song,[a] Luchao Yue,*[a] Xiaoya Fan,[b] Yongsong Luo,[b] Binwu Ying,[b] Shengjun Sun,[c] Dongdong Zheng,[c] Qian Liu,[d] Mohamed S. Hamdy[e] and Xuping Sun*[b,c]

Received 27th March 2023,
Accepted 27th April 2023

DOI: 10.1039/d3qi00554b

rsc.li/frontiers-inorganic

Ammonia ($NH_3$) is an essential raw material in the production of fertilizers and a promising carbon-free energy carrier, however, its synthesis still depends on the energy- and capital-intensive Haber–Bosch process. Recently, the electrochemical $N_2$ reduction reaction has attracted significant interest as an emerging method for $NH_3$ synthesis under ambient conditions. However, the limited solubility of $N_2$ in aqueous electrolyte and the strong $N\equiv N$ bonds result in a low $NH_3$ yield rate, inferior faradaic efficiency and unsatisfactory selectivity, impeding its further practical application. Considering the high water solubility of nitrate ($NO_3^-$), the electrochemical $NO_3^-$ reduction reaction ($NO_3^-RR$) has become a fascinating route for achieving sustainable production of $NH_3$, and enormous progress has been made in this field. As a consequence, this review discusses the reaction mechanism of the electrochemical reduction of $NO_3^-$ and systematically summarizes the recent development of electrocatalysts for the $NO_3^-RR$, including noble-metal-based materials, single-atom metal catalysts, and transition-metal-based catalysts. Diverse design strategies of the catalysts to boost the $NO_3^-RR$ performance, such as defect engineering, rational structure design, strain engineering and constructing heterostructures, are discussed. This is followed by an illustration of how a robust understanding of the optimization strategies affords fundamental insights into the $NH_3$ yield rate, faradaic efficiency, and selectivity of the electrocatalysts. Finally, we conclude with future perspectives on the critical issues, challenges and research directions in the design of high-efficiency electrocatalysts for selective reduction of $NO_3^-$ to $NH_3$.

## 1. Introduction

Ammonia ($NH_3$) as a high-value-added chemical exerts a significant influence in the synthesis of fertilizers for sustaining the rising global population, and is also being considered as a promising alternative fuel for hydrogen storage in the future.[1–3] At present, the synthesis of $NH_3$ in industry mainly hinges on the traditional Haber–Bosch process (HBP). Such a reaction process is accomplished under tough operating conditions, including high temperature (400–550 °C) and high pressure (15–30 MPa), which is extremely energy-consuming.[4,5] Taking the enormous requirements into consideration (~170 Mt per year, over 80% of total content for fertilizers), the HBP consumes 1–2% of the world's energy supply and is accompanied by extensive $CO_2$ emissions.[6] Furthermore, the extensive centralized infrastructures involved in the HBP have to spend substantial capital, leading to a large innovation barrier and uneven regional distribution.[7] In this regard, exploring a clean and sustainable strategy for highly-efficient $NH_3$ production is highly desired, and presents great challenges in both fundamental science and engineering.

Recently, electrochemical $NH_3$ synthesis has provided an alluring research direction in the search for a substitute for the traditional HBP due to its moderate production conditions and ability to integrate with renewable energy resources.[8,9] Among them, the electrochemical $N_2$ reduction reaction (NRR) has drawn tremendous interest and achieved substantial progress. In NRR systems, the electrochemical synthesis of $NH_3$ directly originates from the reduction of $N_2$ and the

---

[a] School of Chemistry and Chemical Engineering & Shanxi Provincial Key Laboratory for High Performance Battery Materials and Devices, North University of China, Taiyuan 030051, Shanxi, China. E-mail: ylctyut@163.com
[b] Institute of Fundamental and Frontier Sciences, University of Electronic Science and Technology of China, Chengdu 610054, Sichuan, China. E-mail: xpsun@uestc.edu.cn, xpsun@sdnu.edu.cn
[c] College of Chemistry, Chemical Engineering and Materials Science, Shandong Normal University, Jinan 250014, Shandong, China
[d] Institute for Advanced Study, Chengdu University, Chengdu 610106, Sichuan, China
[e] Catalysis Research Group (CRG), Department of Chemistry, College of Science, King Khalid University, P.O. Box 9004, 61413 Abha, Saudi Arabia

Published on 02 May 2023. Downloaded on 2/6/2026 6:54:49 PM.

This journal is © the Partner Organisations 2023

Published on 02 May 2023. Downloaded on 2/6/2026 6:54:49 PM.

dissociation of $H_2O$ under ambient conditions, in which the driving force is regulated by the applied voltage.[10–12] Consequently, the thermodynamic energy efficiency of the NRR is about 20% higher than that of the HBP.[1] Meanwhile, this method can achieve the decentralized and on-site/-demand production of $NH_3$, further supporting the fabrication of distributed fertilizers and reducing the cost of transportation. Nevertheless, the highly stable $N{\equiv}N$ bond with a bond energy of 941 kJ $mol^{-1}$, limited solubility of $N_2$, and the competing hydrogen evolution reaction (HER) cause the extremely low $NH_3$ yield rate, selectivity, and faradaic efficiency (FE), which are far from meeting the practical demands, and even result in unreliable quantifications experimentally owing to the trace amounts of contaminants.[13,14]

Recently, the electrochemical nitrate reduction reaction ($NO_3^-RR$) has been demonstrated as an alluring method for $NH_3$ synthesis at room temperature and atmospheric pressure, and its good performance may originate from the following aspects: (i) $NO_3^-$ is highly soluble in water, has a relatively low $N{=}O$ dissociation energy of 204 kJ $mol^{-1}$, and has a more positive potential than $N_2$. These characteristics are beneficial to alleviate the competing HER and attain high $NH_3$ selectivity with only a small overpotential required, indicating that the $NO_3^-RR$ process is more energy-efficient than the HBP and NRR; (ii) $NO_3^-$ is abundant in industrial wastewater and polluted groundwater, with a maximum concentration up to 2.0 mol $L^{-1}$, and these can be considered as $NO_3^-$ sources, providing a promising opportunity for large-scale fabrication of $NH_3$; (iii) converting $NO_3^-$ into $NH_3$ alleviates the environmental degradation caused by excessive nitrate emission and maintains the balance of the perturbed nitrogen cycle. The reason is attributed to the fact that the accumulation of $NO_3^-$ in drinking water will induce illness and jeopardize human health; (iv) this process utilized water as the proton source, eliminating fossil-fuel consumption and $CO_2$ emission. Consequently, there has been a dramatic growth in research efforts to study the ambient electrochemical reduction of $NO_3^-$ to $NH_3$.[15–17] However, the $NO_3^-RR$ is an eight-electron reaction process and generates various by-products, such as $NO_2^-$, NO, $N_2O$, $N_2$, and $NH_2OH$, resulting in low $NH_3$ selectivity, FE and yield rate.[18–20] Such electrocatalytic performance is mainly determined by the electrocatalysts; hence, the major challenge in large-scale production of $NH_3$ *via* the $NO_3^-RR$ lies in finding a suitable catalyst. Recently, a series of electrocatalysts, including noble metals, signal-atom catalysts, and catalysts of transition metals and their compounds have been developed and/or designed for the $NO_3^-RR$ under ambient conditions.[21–24] Meanwhile, extensive research efforts have pointed out that their electrocatalytic activities can be significantly ameliorated by elaborate structural design, defect engineering (oxygen vacancies and heteroatom doping), strain engineering, and constructing heterostructures. Thus, a systematic discussion on the recent progress of electrocatalysts for the $NO_3^-RR$ and an analysis of corresponding materials design principles could provide a specific direction for rationally developing efficient $NO_3^-RR$ electrocatalysts.

Currently, several high-quality reviews focusing on the electrochemical removal of $NO_3^-$ have been presented.[18,19,25,26] Nevertheless, reviews that exclusively focus on the rational design of electrocatalysts for the reduction of $NO_3^-$ to $NH_3$ are lacking. As a consequence, we review the recent advancements of electrocatalysts toward the $NO_3^-RR$ for attaining large $NH_3$ yields, high FE, as well as high selectivity under ambient conditions. Firstly, this review briefly discusses the fundamental reaction mechanisms of the electrocatalytic $NO_3^-RR$. Secondly, the most recent advancements of electrocatalysts for electrochemically converting $NO_3^-$ to $NH_3$ have been summarized, covering noble metals, single-atom catalysts, and catalysts of transition metals and their compounds (Fig. 1a). Meanwhile, several strategies to regulate the apparent activity or intrinsic activity of the electrocatalysts for the $NO_3^-RR$ to form $NH_3$ are highlighted. Finally, the perspective and challenges in this emerging area are also presented.

**Xuping Sun**

*Xuping Sun received his PhD degree from the Changchun Institute of Applied Chemistry (CIAC), Chinese Academy of Sciences, in 2006. From 2006 to 2009, he carried out postdoctoral research at Konstanz University, the University of Toronto, and Purdue University. In 2010, he started his independent research career as a Full Professor at CIAC and then moved to Sichuan University in 2015. In 2018, he joined the University of Electronic Science and Technology of China where he founded the Research Center of Nanocatalysis & Sensing. He was recognized as a highly cited researcher (2018–2020) in both areas of chemistry and materials science by Clarivate Analytics. He has published over 600 papers with total citations of over 63 000 and has a* h*-index of 130. His research mainly focuses on the rational design of nanocatalysts toward applications in electrosynthesis of green hydrogen and ammonia, as well as electrochemical denitration of vehicle exhaust emissions and industrial wastewater.*

## 2. Reaction pathways of electrocatalytic nitrate reduction

Owing to the multivalent nitrogen element, various nitrogen-containing species like $NO_2^-$, $N_2O$, $NH_2ON$, $N_2$, $N_2H_4$, and $NH_3$ will be generated during the electrochemical $NO_3^-$ reduction procedure. Among them, $N_2$ and $NH_3$ feature the highest thermodynamic stability and are regarded as final products under standard conditions.[27,28] The corresponding reactions can be expressed through the following equations:[27]

This journal is © the Partner Organisations 2023

Published on 02 May 2023. Downloaded on 2/6/2026 6:54:49 PM.

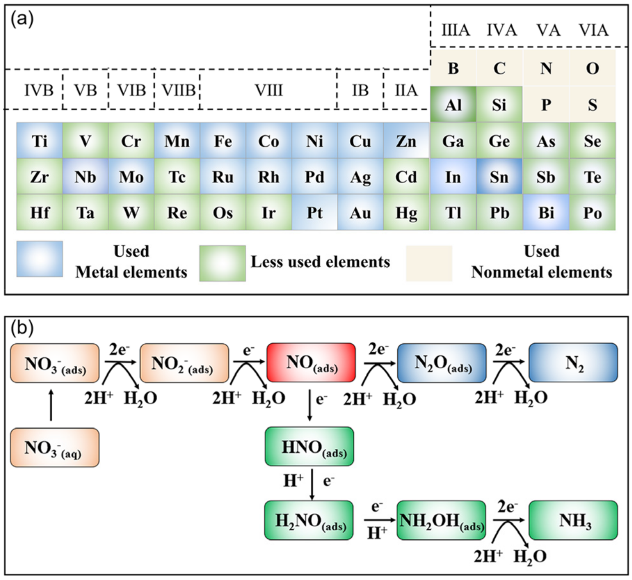

**Fig. 1** (a) Element list of reported $NO_3^-$RR electrocatalysts to date. (b) The electron-mediated pathway of the electrochemical reduction of $NO_3^-$.

$$2NO_3^- + 12H^+ + 10e^- \rightarrow N_2 + 6H_2O, E^\circ = 1.17 \text{ V } vs. \text{ SHE} \tag{1}$$

$$NO_3^- + 9H^+ + 8e^- \rightarrow NH_3 + 3H_2O, E^\circ = -0.12 \text{ V } vs. \text{ SHE}. \tag{2}$$

Generally, the electroreduction of $NO_3^-$ has two different pathways, including an indirect autocatalytic reduction pathway and a direct electrocatalytic reduction pathway.[29–31] In terms of the former, $NO_3^-$ does not participate in the electron-transfer process and the operating conditions are a large concentration of $NO_3^-$ (>1 M) and high acidity (pH < 0). The latter can also be divided into two pathways: one is the regulation of active adsorbed hydrogen atoms ($H_{ads}$); the second one is electron reduction at the cathode (Fig. 1b). In the adsorbed-hydrogen-mediated pathway, the first process is the generation of $H_{ads}$ *via* decomposition of the adsorbed $H_2O$ on the surface of the cathode. The second process is that $H_{ads}$ directly reduces $NO_3^-$ and generates intermediates to give the final-product $NH_3$ rather than $N_2$, which is attributed to the fact that formation of an N–N bond is kinetically less favorable than that of an N–H bond. This process usually requires a small overpotential to promote the conversion from $NO_3^-$ to $NH_3$, which can efficiently suppress the competing HER, as well as attain high $NH_3$ selectivity and FE.[32,33] As for the electron-mediated pathway, electrons directly reduce $NO_3^-$ adsorbed on the surface of the cathode to $NO_2^-$ (eqn (3) and (4)).[34] Notably, converting $NO_3^-$ to $NO_2^-$ generally requires a high activation energy, and this process is considered as the rate-determining step to regulate the reaction kinetics of the whole $NO_3^-$RR process. Then, the generated $NO_2^-{}_{(ads)}$ reduces to $NO_{(ads)}$, which is a decisive intermediate as a branch for the generation of $N_2$ or $NH_3/NH_4^+$. On the one hand, $NO_{(ads)}$ can be reduced to $HNO_{(ads)}$ and $H_2NO_{(ads)}$, and quickly followed by hydrogenation to form hydroxylamine, which finally reduces to $NH_3$.[35] On the other hand, $NO_{(ads)}$ can be desorbed from the electrode surface to generate NO in solution. When $NO_{(aq)}$ presents in the solution, a weakly adsorbed NO dimer can be formed, which is the precursor of $N_2O_{(ads)}$. The produced $N_2O_{(ads)}$ further reduces to $N_2$ according to eqn (9), and this process plays a dominant role in the pathway of $N_2$ evolution.[36,37]

$$NO_3^-{}_{(aq)} \rightarrow NO_3^-{}_{(ads)} \tag{3}$$

$$NO_3^-{}_{(ads)} + 2H^+ + 2e^- \rightarrow NO_2^-{}_{(ads)} + H_2O \tag{4}$$

$$NO_2^-{}_{(ads)} + 2H^+ + e^- \rightarrow NO_{(ads)} + H_2O \tag{5}$$

$$NO_{(ads)} + 6H^+ + 5e^- \rightarrow NH_4^+ + H_2O \tag{6}$$

$$NO_{(ads)} \rightarrow NO_{(aq)} \tag{7}$$

$$NO_{(ads)} + NO_{(aq)} + 2H^+ + 2e^- \rightarrow N_2O_{(ads)} + H_2O \tag{8}$$

$$N_2O_{(ads)} + 2H^+ + 2e^- \rightarrow N_2 + H_2O \tag{9}$$

## 3. Efficient $NO_3^-$RR electrocatalysts

Exploring advanced electrocatalysts with a high selectivity, FE, and yield rate are keenly desired for the electrosynthesis of $NH_3$ by converting $NO_3^-$. Recently, a series of electrocatalysts have been investigated for the $NO_3^-$RR process under ambient conditions, like noble-metal-based materials, single-atom metal catalysts, and transition-metal-based materials. In the following sections, the recent advances of those catalysts in the $NO_3^-$RR toward $NH_3$ and the corresponding optimization strategies for electrocatalytic activity will be systematically discussed.

### 3.1 Noble-metal catalysts

Noble metals have been widely utilized as electrocatalysts for diverse electrochemical conversion reactions including the HER, the oxygen evolution reaction, the oxygen reduction reaction, and the NRR, owing to their alluring electronic conductivity, moderate capturing ability for various reactants, and high density of under-coordinated surface atoms. Recently, both experiments and theoretical calculations have suggested that noble-metal materials (Pt, Pd, Ru, and Rh) are promising electrocatalysts for the $NO_3^-$RR under ambient conditions, as listed in Table 1.[20,38–42,45–48,50,52] For example, Li *et al.*[42] designed Ru/oxygen-doped Ru core/shell nanoclusters (Fig. 2a and b) as an $NO_3^-$RR electrocatalyst for the production of $NH_3$, in which the introduction of oxygen can increase the size of the Ru unit cell to induce tensile strains (Fig. 2c). The strains suppressed the HER but benefit H* production by expanding the barrier of H–H coupling. As a result, this catalyst achieved a large $NH_3$ formation rate of 5.56 mol $g^{-1}$ $h^{-1}$ with a nearly 100% selectivity at 120 mA $cm^{-2}$. In addition, Chen *et al.*[20] dis-

Published on 02 May 2023. Downloaded on 2/6/2026 6:54:49 PM.

**Table 1** Summary of catalytic performance of noble-metal-based electrocatalysts

| Catalyst | Electrolyte | $NH_3$ yield rate | Faradaic efficiency | Potentials (V *vs.* RHE) | Ref. |
|---|---|---|---|---|---|
| Ru-dispersed Cu nanowire | 1 M KOH + 2000 ppm $KNO_3$ | 76 500 $\mu g\ h^{-1}\ cm^{-2}$ | 90% | 0.04 | 20 |
| $BC_2N/Pd$ | 0.1 M KOH + 250 mM $KNO_3$ | 1730 $\mu g\ h^{-1}\ cm^{-2}$ | 97.42% | $-0.7^a/-0.3^b$ | 40 |
| Amorphous Ru nanoclusters | 5 mM $Cs_2CO_3$ + 500 ppm $NO_3^-$ | 145.1 $\mu g\ h^{-1}\ mg^{-1}$ | 80.62% | −0.2 | 41 |
| Strained Ru nanoclusters | 1 M KOH + 1 M $KNO_3$ | 5.56 mol $g_{cat}^{-1}\ h^{-1}$ | 96% | −0.3 | 42 |
| $Pd/Cu_2O$ octahedra | 0.5 M $K_2SO_4$ + 50 ppm $NO_3^-$ | 925.11 $\mu g\ h^{-1}\ mg^{-1}$ | 96.56% | −0.645 | 45 |
| $Pd/Co_3O_4$ | 0.5 M $K_2SO_4$ + 200 ppm $NO_3^-$ | 0.204 mmol $h^{-1}\ cm^{-2}$ | 88.6% | −0.645 | 46 |
| CuPd aerogels | 0.5 M $K_2SO_4$ + 50 mg $L^{-1}$ $NO_3^-$ | 784.37 $\mu g\ h^{-1}\ mg^{-1}$ | 90.02% | −0.46 | 47 |
| CuPd nanocubes | 1 M $KNO_3$ + 1 M KOH | 6.25 mol $h^{-1}\ g^{-1}$ | 92.5% | $-0.6^a/-0.5^b$ | 48 |
| PdBP nanothorn arrays | 0.5 M $K_2SO_4$ + 100 ppm $NO_3^-$ | 0.109 mmol $h^{-1}\ cm^{-2}$ | 64.73% | −0.66 | 50 |
| $RuO_2$ nanosheets | 0.1 M $K_2SO_4$ + 200 ppm $NO_3^-$ | 0.1158 mmol $h^{-1}\ cm^{-2}$ | 97.46% | −0.35 | 52 |

[a] $NH_3$ yield rate. [b] Faradaic efficiency.

persed Ru nanoparticles into a Cu-nanowire matrix (Ru-CuNW) through a simple cation exchange method for electrochemical $NH_3$ synthesis (Fig. 2d). This catalyst presented an industrial-level $NO_3^-$ reduction current of ∼1 A $cm^{-2}$ (Fig. 2e) accompanied by a maximum $NH_3$ FE of 96% (Fig. 2f) when operating with a low $NO_3^-$ concentration of 2000 ppm (typical industrial wastewater). Meanwhile, the voltage of Ru-CuNW does not significantly change during the long-term electrolysis of 100 h under the current density of 400 mA $cm^{-2}$, with a high $NH_3$ FE of 90% maintained, indicating that such a catalyst features excellent durability. More importantly, it showed an ultrahigh $NO_3^-$ conversion ratio of 99% for $NH_3$ production, making industrial wastewater reach a drinkable water level (concentration of $NO_3^- < 50$ ppm) (Fig. 2g), and the solid $NH_4Cl$ and liquid $NH_3$ solution products were collected by coupling the $NO_3^-$-reduction effluent stream with the air-stripping process, as displayed in Fig. 2h. In another study, Jiang *et al.*[41] investigated the effect of the noble-metal crystal structure on electrochemical $NO_3^-$RR activity. They chose Ru as the model material and fabricated amorphous Ru nanoclusters anchored on carbon nanotubes (aRu-CNTs) for electrochemical $NH_3$ production from $NO_3^-$. The experimental results demonstrated that aRu-CNTs delivered an $NH_3$ yield of 145 μg $h^{-1}$ $mg^{-1}$ with a FE of 80.62% at −0.2 V *vs.* RHE, and the achieved yield was 3.1 times larger than that of crystalline Ru. Therefore, the amorphization of noble metals can be recognized as a promising route for increasing the amount of active sites on the catalysts to a certain degree.

Besides, revealing the electrocatalytic behaviors on noble metals with different facets for the $NO_3^-$RR is essential to explore rational design strategies for electrosynthesis of $NH_3$. Lim *et al.*[43] employed Pd as a model catalyst to understand the structure-sensitivity of $NO_3^-$ reduction to $NH_3$ on a Pd catalyst. Specifically, they fabricated Pd nanoparticles with diverse morphologies, such as nanocubes containing six (100) facets, cuboctahedrons containing six (100) and eight (111) facets, octahedrons containing eight (111) facets, and concave nanocubes containing (100) and (*hk*0) facets. Based on the experimental results, the Pd (111) facet is favorable to catalyze the reduction of $NO_3^-$ to $NO_2^-$, while the (100) facet is inclined to catalyze the reduction of $NO_2^-$ to $NH_3$ (Fig. 2i–k). Hence, the activity for $NO_3^-$ reduction decreases in the order of Pd (111) > Pd (100) > Pd (*hk*0) and the activity for $NO_2^-$ reduction decreases in the order of Pd (100) > Pd (*hk*0) > Pd (111) under the alkaline electrolyte. As a consequence, $NH_3$ production using noble-metal catalysts can be enhanced through controlling their structure and facets.

Numerous research studies have demonstrated that the electrochemical performance of noble metals for converting $NO_3^-$ to $NH_3$ can be significantly modified by constructing a heterostructure with two materials, with the modified performance originating from the unique physical properties induced by the charge distribution and energy-band bending at the heterointerface. For instance, Li *et al.*[40] constructed a hybrid material consisting of Pd nanoparticles and a boron–carbon–nitrogen material ($BC_2N/Pd$) for the $NO_3^-$RR, which showed a superior $NH_3$ production rate of 1730 μg $h^{-1}$ $cm^{-2}$ at −0.7 V *vs.* RHE using 250 mM $KNO_3$ solution as the nitrogen source. Theoretical calculations revealed that the free energy accumulation of the $NO_3^-$RR on $BC_2N/Pd$ was higher than that of individual Pd or $BC_2N$, and the corresponding value from $NO_3^-$ to *NH could conquer the reaction energy barriers from *NH to $*NH_2$ and $*NH_2$ to $NH_3$. As exhibited in Fig. 3a–d, Ren *et al.*[44] constructed $Cu/Pd/CuO_x$ heterostructures with abundant pores for electrochemical conversion of $NO_3^-$ to $NH_3$. In terms of the $Cu/Pd/CuO_x$ heterostructure, the electronic interactions between the Cu, Pd, and $CuO_x$ components lead to electron transfer from Pd to Cu, which can increase the number of reactive sites and thus modulate the adsorption ability for intermediates, meanwhile suppressing the competitive hydrogen evolution reaction process. Moreover, the abundant channels provided sufficient contact area between electrolyte and catalyst. Benefiting from interfacial engineering and a unique porous structure, the designed $Cu/Pd/CuO_x$ heterostructure afforded a superior $NH_3$ production rate of 1510.3 μg $h^{-1}$ $mg^{-1}$, FE of 86.1%, and $NH_3$ selectivity of 90.06% (Fig. 3e–f). Similarly, Xu *et al.*[45] applied $Cu_2O$ corner-etched octahedra with cavities and oxygen defects as the substrate to support Pd nanoparticles ($Pd-Cu_2O$), in which the loading content of Pd active materials was only 2.93%. For $Pd-Cu_2O$ catalyst system, Pd sites were regarded as the active center for capturing *H and generating Pd–H intermediate; while parts of $Cu_2O$ elec-

Published on 02 May 2023. Downloaded on 2/6/2026 6:54:49 PM.

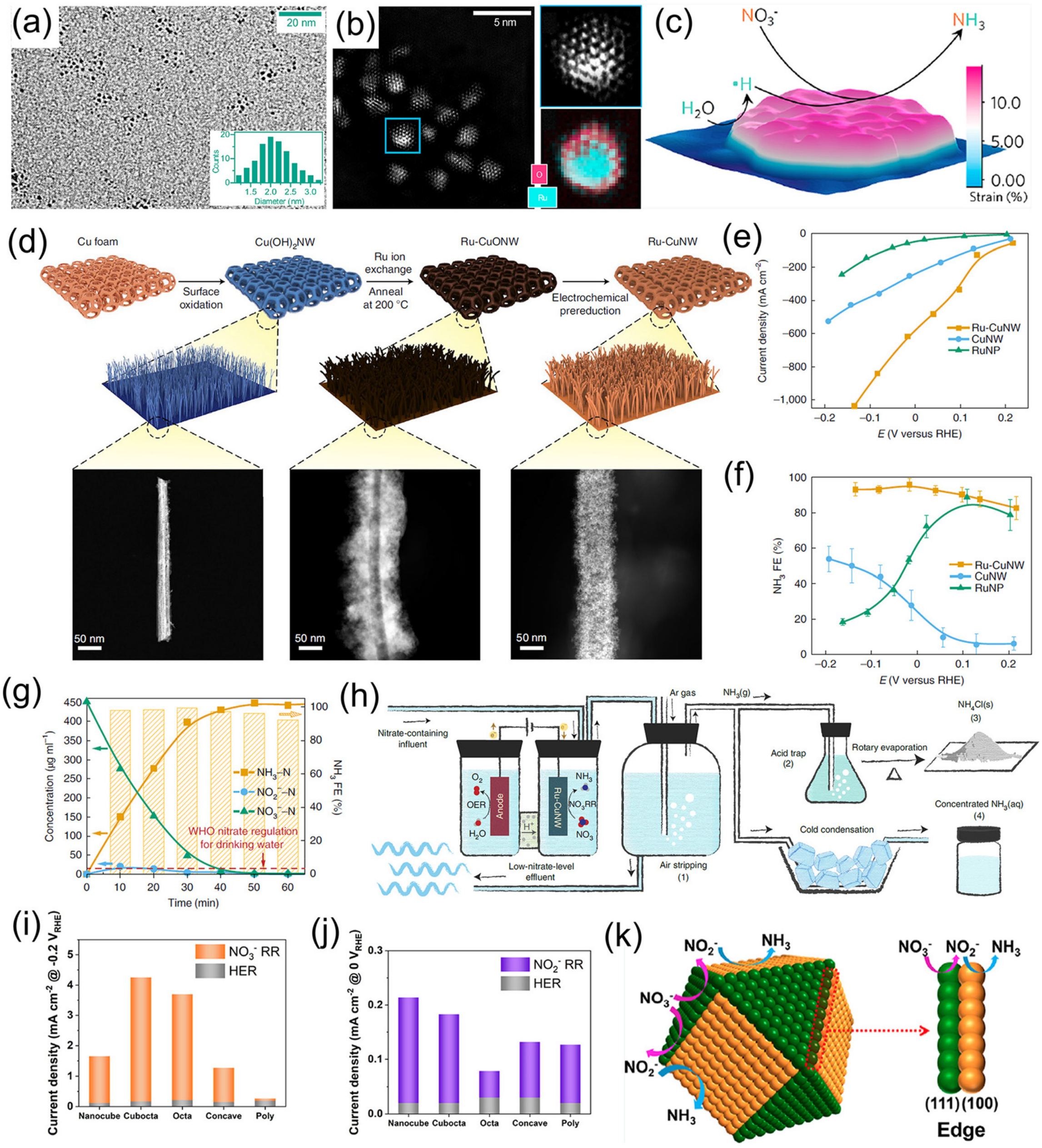

**Fig. 2** (a) TEM image and (b) aberration-corrected HAADF-STEM/EELS elemental map images of Ru/oxygen-doped Ru core/shell nanoclusters. (c) Schematic illustration of the reaction mechanism for the $NO_3^-$RR on the strained Ru nanoclusters. Reproduced from ref. 42 with permission from the American Chemical Society, copyright 2020. (d) Synthesis process of the Ru-CuNW catalyst. (e and f) *I*–*V* plots and corresponding $NH_3$ FEs of Ru-CuNW and counterparts. (g) Complete $NO_3^-$ removal using Ru-CuNW catalyst. (h) Schematic diagram of $NH_4Cl_{(s)}$ and concentrated $NH_{3(aq)}$ products from nitrate-containing influent. Reproduced from ref. 20 with permission from the Nature Publishing Group, copyright 2022. (i and j) The electrocatalytic activity of Pd catalysts with various structures. (k) Schematic illustration of the reaction mechanism for the $NO_3^-$RR on the different crystal facets of Pd catalysts. Reproduced from ref. 43 with permission from the American Chemical Society, copyright 2021.

trochemically reduced to $Cu^0$ and *in situ* formed $Cu/Cu^+$, which could provide active sites for $NO_3^-$ electroreduction. Meanwhile, the oxygen defects in $Cu_2O$ were beneficial for the capture of $NO_3^-$ and to weaken the N–O bond. As expected, $Pd/Cu_2O$ heterostructure catalyst exhibited an excellent electrocatalytic activity of $NO_3^-$ to $NH_3$, including $NH_3$ formation rate of 925.11 μg h$^{-1}$ mg$^{-1}$, selectivity of 95.31%, and FE of 96.56%. Pd-PdO-modified $Co_3O_4$ nanowire arrays were fabricated and applied as a catalyst to electrochemically convert $NO_3^-$ to $NH_3$. In $K_2SO_4$ solution containing 200 mg L$^{-1}$ of $NO_3^-$ electrolyte, such catalyst showed a high $NH_3$ FE of 88.6% and selectivity of 95.3%.[46]

Tailoring the catalytic sites of noble-metal materials by alloying with another metal is another fascinating strategy to

Published on 02 May 2023. Downloaded on 2/6/2026 6:54:49 PM.

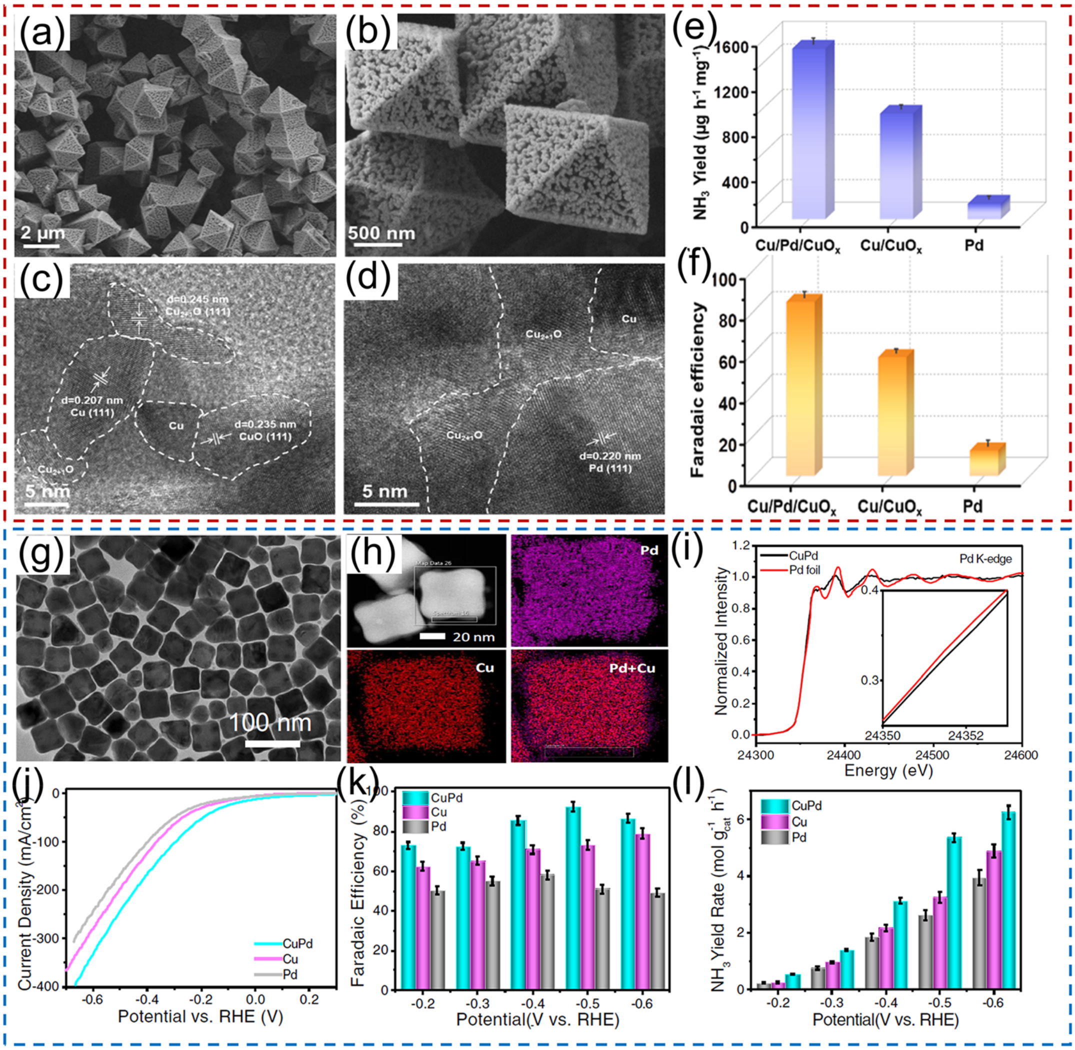

Fig. 3 (a–d) TEM and HRTEM images of Pd/CuO material. (e) $NH_3$ yield rate and (f) the corresponding FE of Pd/CuO catalyst. Reproduced from ref. 44 with permission from Elsevier, copyright 2022. (g and h) TEM and mapping images of the CuPd alloy. (i) Pd K-edge XANES spectra of CuPd and a Pd foil reference. (j) Linear scan voltammetry (LSV) curves, (k) $NH_3$ FE and (l) $NH_3$ yield rate under different potentials for CuPd, Cu, and Pd. Reproduced from ref. 48 with permission from the Nature Publishing Group, copyright 2022.

further improve their catalytic activity for the $NO_3^-$RR to $NH_3$. For example, Xu *et al.*[47] rationally chose Pd as an active metal and Cu as a promoting metal to construct a CuPd bimetallic catalyst for electrochemical conversion of $NO_3^-$ to $NH_3$. In terms of the CuPd catalyst system, Pd sites serve as active centers to adsorb *H and promote the hydrogenation reaction for $NH_3$ production. Consequently, the CuPd alloy catalyst delivered a large $NH_3$ yield rate of 784.37 μg $h^{-1}$ $mg^{-1}$, and a high $NH_3$ FE of 90.02% at −0.46 V *vs.* RHE, which was superior to those of pure Cu and Pd catalysts. Furthermore, Gao *et al.*[48] employed density functional theory (DFT) calculations and machine learning to deduce that the upshifted d-band center of the Cu sites of the CuPd alloy favored the adsorption of *$NO_3$, and *N was destabilized owing to the dominant role of Pauli repulsion from the subsequent Pd d orbitals, promoting the protonation of N-bonded species toward $NH_3$. As demonstrated in Fig. 3g–l, they also experimentally synthesized CuPd nanocube alloy catalysts, and confirmed the existence of charge transfer between Pd and Cu *via* X-ray absorption near-edge spectroscopy (XANES). In 1.0 M NaOH solution containing 1.0 M $KNO_3$, the PdCu nanocube catalyst showed an $NH_3$ yield rate of 6.25 mol $h^{-1}$ $g^{-1}$ at −0.6 V *vs.* RHE and an $NH_3$ FE of 92.5% at −0.5 V *vs.* RHE, respectively. Furthermore, the current density remained stable over 12 h of continuous operation, with a high $NH_3$ FE of ~85.1% maintained. Similarly, Zhang and his co-authors[49] also employed metallic Ni as a promoter catalyst to regulate the electronic structure of Pd, and synthesized PdNi alloys for the $NO_3^-$RR. PdNi nanosheets displayed an $NH_3$ formation rate of 16.7 mg $h^{-1}$ $mg^{-1}$ (at −1.2 V *vs.* RHE) and a FE of 87.9% (at −0.6 V *vs.* RHE). After that, a ternary PdBP nanothorn-array catalyst was also designed and utilized for converting $NO_3^-$ to $NH_3$. In terms of the ternary system, B and P doping could induce the lattice strain, thus regulating the electronic structure and increasing the number

View Article Online

Published on 02 May 2023. Downloaded on 2/6/2026 6:54:49 PM.

of active sites of Pd; in addition, the doping sites also served as the Lewis acid to improve the adsorption ability for $NO_3^-$. Thus, the electrochemical performance for reducing $NO_3^-$ to $NH_3$ was significantly enhanced after B and P doping.[50]

Several noble-metal oxides were also used as electrocatalysts for highly efficient $NH_3$ formation by electrochemical conversion of $NO_3^-$ at room temperature. Liu *et al.*[51] fabricated oxide-derived silver and investigated its electrochemical activity for the $NO_3^-$RR. It is noted that this catalyst delivered excellent electrocatalytic activity of $NO_3^-$ to $NO_2^-$ and thus promoted the reduction reaction of $NO_2^-$ to $NH_4^+$, which was well controlled by the applied potential and they obtained an $NH_4^+$ FE of 89%. Qin *et al.*[52] designed and synthesized $Ru_xO_y$ clusters anchored on nickel metal–organic frameworks (MOF) for the $NO_3^-$RR. Such a catalyst could provide a nearly 100% $NH_4^+$ selectivity with an $NH_4^+$ yield rate of 274 μg $h^{-1}$ $mg^{-1}$. Wang *et al.*[53] fabricated carbon-supported $RuO_2$ nanosheets with abundant oxygen vacancies for electrochemical $NO_3^-$ to $NH_3$ conversion. The abundant oxygen vacancies within the $RuO_2$ nanosheets could regulate the d-band center and improve the hydrogen affinity, thus reducing the reaction-energy barrier of the potential-determining step ($NH_2^* - NH_3^*$). As a result, this catalyst displayed a superior electrocatalytic activity for the conversion of $NO_3^-$to $NH_3$ ($NH_3$ FE of 97.46% and selectivity of 96.42%) than that of the crystalline counterparts.

### 3.2 Single-atom catalysts

Single-atom catalysts, a group of emerging frontier materials comprising isolated metal atoms dispersed into support materials, have triggered explosive research interest within the catalysis field owing to their remarkably high catalytic activity and selectivity. When applied to the $NO_3^-$RR, single-atom catalysts can provide the following desirable advantages, including (i) the specific atomic structure can expose abundant adsorption sites and homogenous catalytic active centers; (ii) the strong interactions between single atoms and the surrounding atoms enable superior long-term electrolysis; and (iii) the absence of multiple neighboring active sites required for coupling N–N bonds in their structure can efficiently suppress the generation of by-product $N_2$, thus enhancing $NH_3$ selectivity. Currently, both experimental and theoretical calculations have suggested that single-atom catalysts are effective toward electroreduction of $NO_3^-$ to $NH_3$.

For example, Niu and co-workers[54] used first-principle calculations to systematically investigate the electrocatalytic activity of various transition-metal single-atoms (from Ti to Au) anchored on carbon nitride (TM/g-CN) for electrochemical $NO_3^-$ to $NH_3$ conversion, as shown in Fig. 4a. Firstly, the adsorption energies of $NO_3^-$, a H proton, and an $N_2$ molecule on TM/g-CN were systematically calculated. As revealed from Fig. 4b, the adsorption ability for $NO_3^-$ was stronger than for H proton or $N_2$ on TM/g-CN catalysts, except for Pt and Au, indicating that the $NO_3^-$RR is more favorable than the HER and NRR. By combining with detailed pathways of $NO_3^-$ reduction on TM/g-CN, they established a volcano plot of limiting potential selecting the adsorption energy of $NO_3^-$ as a descriptor (Fig. 4c), where Ti and Zr appeared near the top of the volcano. Based on the above analysis, Ti/g-CN and Zr/g-CN possessed stronger adsorption abilities for $NO_3^-$ compared with those of other TM/g-CN catalysts, making them fascinating electrocatalysts with high activity and selectivity for the $NO_3^-$RR. Similarly, Lv *et al.*[55] explored the $NO_3^-$RR performance of a set of transition-metal single-atom (Ti, Os, Ru, Cr, Mn, and Pt) catalysts supported on g-$C_3N_4$ by performing DFT calculations. The calculation results suggested that Ru/g-$C_3N_4$ featured the highest activity and selectivity for the conversion

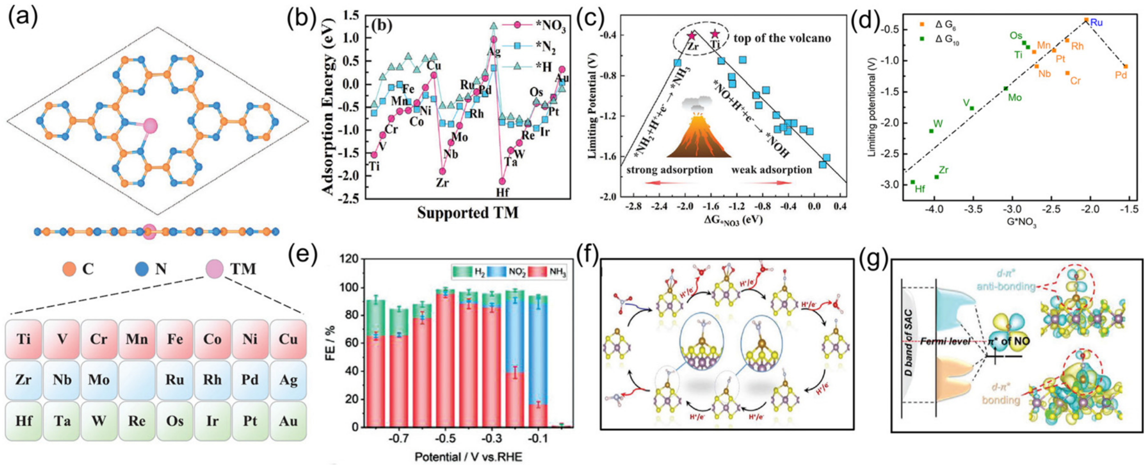

Fig. 4 (a) Atomic structure of TM/g-CN and corresponding element list (from Ti to Au). (b) Comparison of adsorption energies of $NO_3^-$, $N_2$, and H proton on TM/g-CN. (c) $NO_3^-$RR volcano plot of TM/g-CN using the adsorption energy of $NO_3^-$ as the descriptor. Reproduced from ref. 54 with permission from Wiley-VCH, copyright 2021. (d) Volcano correlation curve between the limiting potential and adsorption energy of $NO_3^-$ of TM/g-$C_3N_4$. Reproduced from ref. 55 with permission from the American Chemical Society, copyright 2021. (e) $NH_3$ FE of Fe-$MoS_2$ under various potentials. (f) Reaction pathway for the $NO_3^-$RR on Fe-$MoS_2$. (g) Schematic diagram of the interaction between NO and M-$MoS_2$ nanosheets. Reproduced from ref. 57 with permission from Wiley-VCH, copyright 2022.

Published on 02 May 2023. Downloaded on 2/6/2026 6:54:49 PM.

Table 2 Summary of catalytic performance of single-atom metal electrocatalysts

| Catalyst | Electrolyte | $NH_3$ yield rate | Faradaic efficiency | Potentials (V *vs.* RHE) | Ref. |
|---|---|---|---|---|---|
| Fe-$MoS_2$ SAC | 0.1 M $Na_2SO_4$ + 0.1 M $NaNO_3$ | 431.8 μg $h^{-1}$ $cm^{-2}$ | 98% | −0.48 | 57 |
| Fe SAC | 0.1 M $K_2SO_4$ + 0.5 M $NO_3^-$ | 0.46 mmol $h^{-1}$ $cm^{-2}$ | 75% | $-0.85^a/-0.66^b$ | 58 |
| Fe-PPy SAC | 0.1 M KOH + 0.1 M $NO_3^-$ | 2.75 mg $h^{-1}$ $cm^{-2}$ | 100% | −0.7/−0.3 | 59 |
| Cu SAC | 0.1 M KOH + 0.1 M $NO_3^-$ | 4.5 mg $cm^{-2}$ $h^{-1}$ | 84.7% | −1.0 | 60 |
| Cu-*cis*-$N_2O_2$ SAC | 0.5 M $K_2SO_4$ + 1000 ppm $NO_3^-$ | 28.73 ± 1.25 mg $h^{-1}$ $cm^{-2}$ | 80% | −1.6 | 61 |
| $FeN_2O_4$ SAC | 0.1 M $K_2SO_4$ + 0.5 M $NO_3^-$ | 46 mg $h^{-1}$ $mg^{-1}$ | 92% | $-0.88^a/-0.68^b$ | 62 |
| Ni-Cu SAC | 0.5 M $K_2SO_4$ + 200 ppm $NO_3^-$ | 326.7 μmol $h^{-1}$ $cm^{-2}$ | 100% | −0.55 | 63 |
| FeMo SAC | 0.05 M PBS + 0.16 M $KNO_3$ | 18.0 μmol $cm^{-2}$ $h^{-1}$ | 94% | −0.45 | 64 |

[a] $NH_3$ yield rate. [b] Faradaic efficiency.

of $NO_3^-$ to $NH_3$ with a limiting potential of −0.34 V, as presented in Fig. 4d. Thus, theoretical calculations have provided an advanced direction for the application of single-atom catalysts and paved the way for the electrochemical conversion of $NO_3^-$ to $NH_3$.

Up to now, only a few single-atom catalysts have been experimentally fabricated and employed for the electrosynthesis of $NH_3$ from $NO_3^-$, including Fe, Cu, Ni, Mo, and their alloys, as listed in Table 2. For example, Zhu *et al.*[56] prepared a single-atom Cu-catalyst supported on nitrogenated carbon nanosheets (Cu–N–C) and investigated its catalytic performance for the $NO_3^-$RR for the first time. The strong binding between Cu and N (Cu–$N_2$) was responsible for the good adsorption ability of the catalyst for $NO_3^-$ adsorption, promoting the fast conversion from $NO_3^-$ to $NH_3$ as well as exhibiting excellent stability. Furthermore, Chen *et al.*[24] demonstrated that Cu–N–C could effectively inhibit the generation of toxic $NO_2^-$ and by-product $N_2$, as well as facilitate the reduction of $HNO_3^*$ to $NO_2^*$, and $NH_2^*$ to $NH_3^*$. It is well known that the nitrate reductase enzyme has a Mo(IV) atom coordinated with sulfur coordinating ligands, whereas nitrogenase is a multinuclear enzyme with $MoFe_7$ clusters as the active sites. Inspired by this point, Voiry's group[57] developed a novel heterogeneous catalyst composed of Fe single-atoms anchored on two-dimensional $MoS_2$ (Fe-$MoS_2$) for electrochemical $NH_3$ synthesis by the reduction reaction of $NO_3^-$. Fe-$MoS_2$ delivered a remarkably high FE of 98% for the $NO_3^-$RR to $NH_3$ at an onset potential of −0.48 V using 0.1 M $Na_2SO_4$ containing 0.1 M $NaNO_3$ electrolyte (Fig. 4e). Under the above testing conditions, this catalyst showed a 7-hour average $NH_3$ formation rate of 431.8 μg $h^{-1}$ $cm^{-2}$. DFT calculations revealed that the Fe-$MoS_2$ catalyst featured a superior ability for activating $NO_3^-$ by virtue of the strong interaction between the d-band orbitals of the Fe atoms and the $2\pi^*$ orbitals of the NO species, lowering the energy barrier for conversion of *NO to *N (the rate-determining step) (Fig. 4f and g). At the same time, Wu *et al.*[58] chose an N-doped porous carbon matrix to anchor Fe single-atoms (Fe SAC) and applied them for electrochemical $NO_3^-$ to $NH_3$ conversion (Fig. 5a and b). A large $NH_3$ yield rate (up to 0.46 mmol $h^{-1}$ $cm^{-2}$ at −0.85 V *vs.* RHE) and a high $NH_3$ FE of 75% at −0.66 V *vs.* RHE were achieved in $K_2SO_4$ with 0.5 M $KNO_3$, and remained stable during 20 consecutive electrolysis cycles (Fig. 5c–e). These results indicated that Fe SAC featured superior electrocatalytic activity and outstanding durability for the $NO_3^-$RR. The favorable catalytic activity of the as-designed Fe SAC originated from the unique structure, which can not only effectively suppress the N–N coupling and enhance the selectivity of $NH_3$ production, but also enable the intrinsic high-efficiency active sites (Fe–$N_4$) to possess lower thermodynamic barriers. However, the detailed reaction mechanism of Fe SAC was only revealed through theoretical modeling. During the electrocatalytic reaction process, the M (metal)–$N_x$ catalyst may experience structural evolution induced by the applied potential and/or the interaction with reactants or electrolytes, which complicates the comprehension of the structure–performance relationship and seriously blocks the rational design of efficient catalysts. Consequently, revealing the dynamic transformation of the M–$N_x$ structure under operating conditions is essential to recognize the real active sites. To achieve the above-mentioned target, Li *et al.*[59] employed *in situ* characterisation techniques to establish the reaction pathway and evolution mechanism of the catalysts, selecting a catalyst of Fe single atoms anchored on carbon derived from polypyrrole as an example. They proposed the preoccupied $NO_3^-$RR mechanism presented in Fig. 5f that the exclusive existence of nitrate-preoccupied Fe(II)–$N_x$ sites prior to the formation of Fe (0), which could effectively eliminate the competing adsorption of water under aqueous conditions. Subsequently, Yang *et al.*[60] discovered the restructuring of Cu–$N_4$ sites during the electrochemical production of $NH_3$ by converting $NO_3^-$ through *in situ* X-ray adsorption spectroscopy coupled with advanced electron microscopy. Specifically, as depicted in Fig. 5g–i, the Cu–$N_4$ structure experienced the sequential evolution from Cu–$N_3$ to near-free $Cu^0$ single atoms and finally to aggregated $Cu^0$ nanoparticles during the electroreduction of $NO_3^-$ to $NH_3$. Moreover, the formed $Cu^0$ nanoparticles can be dismantled into single atoms and again recovered to give the Cu–$N_4$ structure upon being exposed to an ambient atmosphere after the electrolysis.

Although single-atom catalysts deliver outstanding electrocatalytic activity for the conversion of $NO_3^-$ to $NH_3$, the isolated metal centers usually coordinate with four N atoms in $C_{4V}$ symmetry. Such a coordination structure features relatively weak adsorption ability for $NO_3^-$, leading to sluggish ionic

This journal is © the Partner Organisations 2023

Published on 02 May 2023. Downloaded on 2/6/2026 6:54:49 PM.

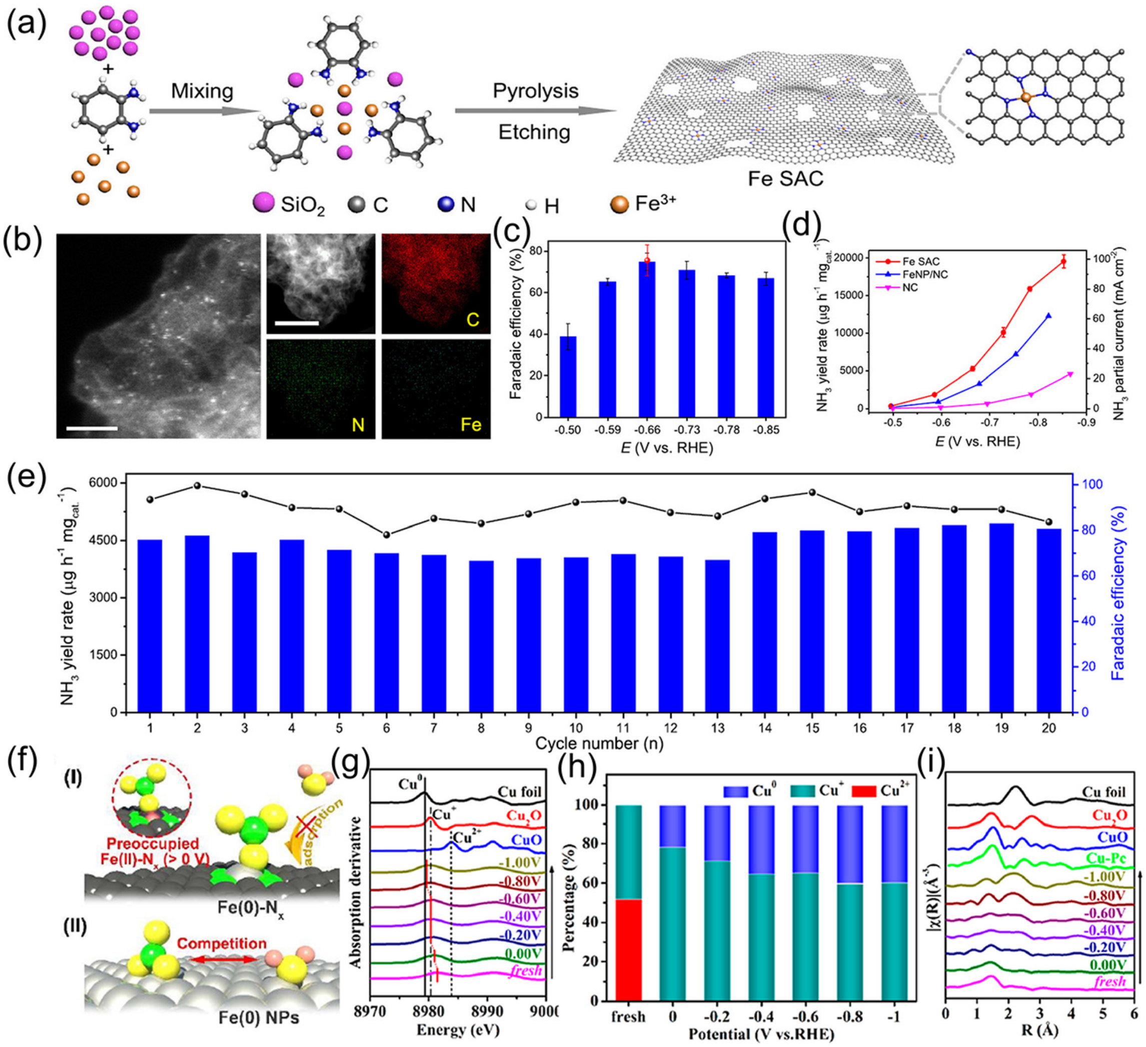

**Fig. 5** (a) Schematic illustration of the preparation of Fe SAC. (b) Aberration-corrected medium-angle annular dark-field scanning TEM (HAADF STEM) and mapping images of Fe SAC. (c) $NH_3$ FE. (d) $NH_3$ yield rate and partial current density of Fe SAC under various potentials. (e) Cycling durability of Fe SAC at −0.66 V *vs.* RHE. Reproduced from ref. 58 with permission from the Nature Publishing Group, copyright 2021. (f) The proposed preoccupied $NO_3^-$RR mechanism for Fe SAC. Reproduced from ref. 59 with permission from The Royal Society of Chemistry, copyright 2021. (g) *In situ* XANES spectra of Cu–$N_4$ at each given potential. (h) Linear combination fitting result of the Cu K-edge XANES spectra and (i) corresponding Cu K-edge FT-EXAFS spectra at different potentials. Reproduced from ref. 60 with permission from the American Chemical Society, copyright 2022.

migration and low $NH_3$ production rate. Related literature has demonstrated that introducing weakly coordinated heteroatoms to substitute some of the coordinated N is an admirable strategy for breaking the coordination symmetry of the metal centers, consequently increasing the site polarity and improving $NO_3^-$ accumulation. For instance, Cheng *et al.*[61] broke the coordination symmetry of Cu SAC by replacing the local coordination atoms from 4N to 2N + 2O (Cu-*cis*-$N_2O_2$). First-principle calculations were preferentially employed to reveal the coordination symmetry-breaking in Cu SAC and investigate the reaction pathways of Cu-*cis*-$N_2O_2$ and Cu–$N_4$ catalysts, as indicated in Fig. 6a–e. In terms of Cu-*cis*-$N_2O_2$, Cu is coordinated by two N and two O atoms and the catalyst possesses polar active sites, which are prone to enrich $NO_3^-$ on the surface of the catalyst and promote the generation of the key reaction intermediate *ONH, further facilitating hydrogenation to $NH_3$. Motivated by this, a Cu-*cis*-$N_2O_2$ catalyst was fabricated by pyrolysis of a Cu–Salen complex under an Ar atmosphere (Fig. 6g–h). When applied to the $NO_3^-$RR, the $NH_3$ formation rate reached 27.84 mg $h^{-1}$ $cm^{-2}$ at an industrial-level current density of 366 mA $cm^{-2}$. Moreover, the electrochemical activity of Cu-*cis*-$N_2O_2$ was well maintained after continual operation for 2000 h (Fig. 6i–k). Analogously, Zhang *et al.*[62] fabricated an Fe single-atom catalyst with unique $FeN_2O_2$ coordination *via* direct pyrolysis of metal–organic frameworks possessing a pre-organized $FeN_2O_4$ environment. When applying the designed Fe SAC for the $NO_3^-$RR, it showed a high $NH_3$ production rate of 46 mg $h^{-1}$ $mg^{-1}$ with a FE of 92% in neutral electrolytes. Combined theoretical calculations revealed that the O atoms in $FeN_2O_2$ could regulate the d-band center of Fe and conse-

Published on 02 May 2023. Downloaded on 2/6/2026 6:54:49 PM.

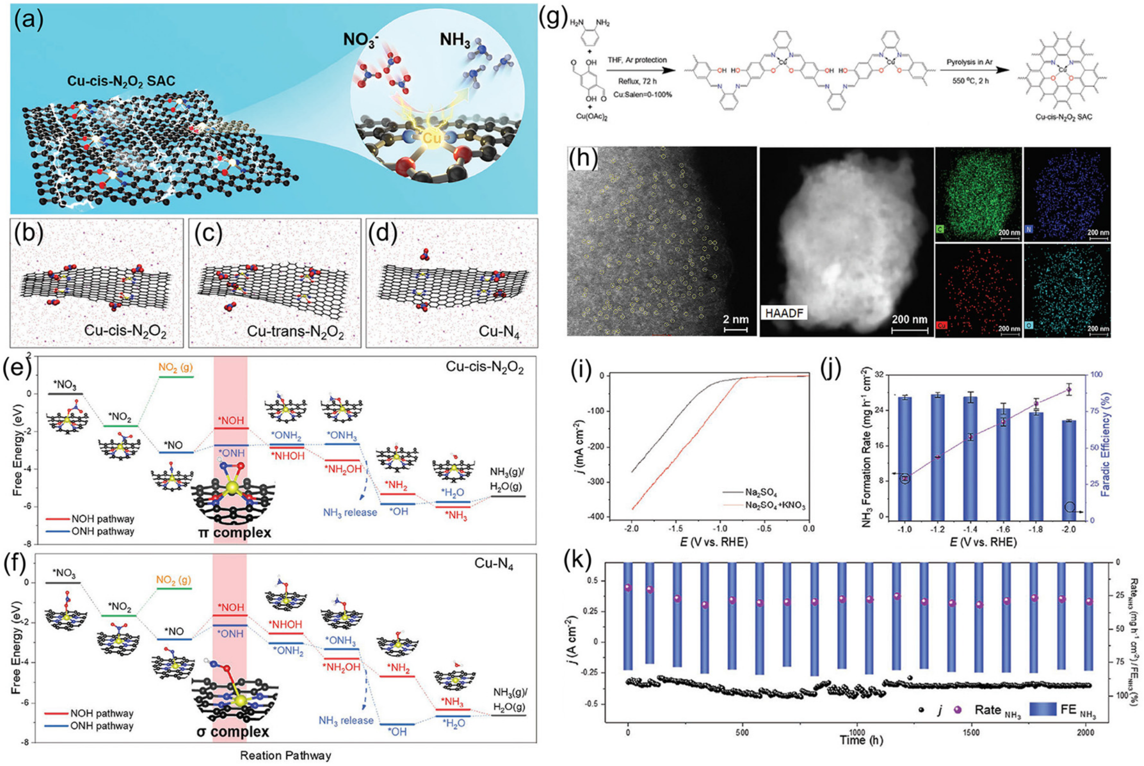

**Fig. 6** (a) Illustration of the Cu-*cis*-$N_2O_2$ catalyst. (b–d) The molecular dynamic simulation of Cu-*cis*-$N_2O_2$ and counterparts. (e and f) Reaction pathways for the $NO_3^-$RR on the surface of Cu-*cis*-$N_2O_2$ and Cu-$N_4$. (g) Synthesis process of Cu-*cis*-$N_2O_2$. (h) HAADF STEM and corresponding mapping images of Cu-*cis*-$N_2O_2$. (i) LSV curves, (j) $NH_3$ formation rate and FE at each given potential. (k) Cycling stability test of Cu-*cis*-$N_2O_2$. Reproduced from ref. 61 with permission from Wiley-VCH, copyright 2022.

quently enhance the adsorption energies of the $NO_3^-$RR intermediates. In comparison with $FeN_4$, $FeN_2O_2$ features superior conductivity, $NH_3$ selectivity and a lower reaction energy barrier from *NOH to *N, thus promoting the progress of the $NO_3^-$RR.

To further enhance the catalytic activity of single-atom catalysts, tuning the electronic structures of active sites through introducing foreign atoms in the metal matrix can be regarded as an alluring approach to increase the $NH_3$ production rate, selectivity and FE. For example, Cai *et al.*[63] reported a single-atom Ni-alloyed Cu catalyst that achieved an $NH_3$ yield rate of 326.7 μmol $h^{-1}$ $cm^{-2}$ at −0.55 V *vs.* RHE and a maximum FE of 100% in 0.5 M $K_2SO_4$ with 200 ppm $NO_3^-$, in which the yield rate was nearly 10.7 times superior to that of a bare Cu catalyst. Theoretical calculations suggested that the single Ni atom on the Cu catalyst regulated the third protonation reaction of the electrocatalytic $NO_3^-$RR and increased the adsorption energy of the crucial NOOH* intermediate, thus decreasing the limiting potential and inhibiting the formation of by-product. Murphy *et al.*[64] reported a bimetallic FeMo-based single-atom catalyst for electroreduction of $NO_3^-$ to $NH_3$, in which Mo and Fe served as the dissociative and associative sites of the initial adsorption of $NO_3^-$, respectively. Benefiting from the synergistic effect of both Mo and Fe sites, this bimetallic catalyst achieved an $NH_3$ production rate of 18.0 μmol $cm^{-2}$ $h^{-1}$ (153 $μg_{NH_3}$ $mg^{-1}$ $h^{-1}$) with a FE of 94%, as well as outstanding long-term durability with a well-maintained FE above 90% for over 60 h of electrolysis.

In the above-mentioned two parts, we have discussed noble-metal and single-atom metal catalysts for conversion of $NO_3^-$ to $NH_3$ under ambient conditions. Although an extensive number of electrocatalysts deliver desirable activity, high FE and superior selectivity, their large-scale practical application is still impeded by their expensive cost, rare resources (noble metals) and low yield (single-atom catalysts). In contrast, non-noble transition metals, such as Cu, Co, Ni, Fe, and their alloys, have drawn extensive attention as promising alternatives in the field of electrochemical conversion of $NO_3^-$ to $NH_3$ by virtue of their abundant resources and favorable catalytic activity. Transition-metal-based materials including metals, metal oxides, metal phosphides, and so on, have been widely investigated as highly efficient catalysts for the $NO_3^-$RR. In the following section, the recent advances in transition-metal-based electrocatalysts for the $NO_3^-$RR will be systematically discussed.

### 3.3 Transition-metal catalysts

**3.3.1 Zero-metal catalysts.** Owing to the similar energy levels between the d orbitals of Cu and the LUMO π* molecular orbital of $NO_3^-$, metallic Cu catalysts have attracted extensive

Published on 02 May 2023. Downloaded on 2/6/2026 6:54:49 PM.

Table 3 Summary of catalytic performance of transition-metal electrocatalysts

| Catalyst | Electrolyte | $NH_3$ yield rate | Faradaic efficiency | Potentials (V *vs.* RHE) | Ref. |
|---|---|---|---|---|---|
| Cu nanosheets | 0.1 M KOH + 10 mM $KNO_3$ | 390.1 μg $mg^{-1}$ $h^{-1}$ | 99.7% | −0.15 | 70 |
| Cu polycrystalline | 0.5 M $Na_2SO_4$ + 0.1 M $KNO_3$ | 101.4 μmol $h^{-1}$ $cm^{-2}$ | 93.91% | −0.266 | 71 |
| dr-Cu nanoplates | 0.5 M $K_2SO_4$ + 50 ppm $KNO_3^-$ | 781.25 μg $h^{-1}$ $mg^{-1}$ | 85.47% | −0.654 | 72 |
| Cu with grain boundaries | 0.1 M KOH + 10 mM $NO_3^-$ | 487.8 mmol $g^{-1}$ $h^{-1}$ | 94.2% | −0.2 | 74 |
| Cu@C | 0.1 M KOH + 1 mM $NO_3^-$ | 469.5 μg $h^{-1}$ $cm^{-2}$ | 72.0% | $-0.9^a/-0.3^b$ | 77 |
| Cu/$TiO_{2-x}$ | 0.5 M $Na_2SO_4$ + 500 ppm $NO_3^-$ | 0.1143 mmol $h^{-1}$ $mg^{-1}$ | 81.34% | −0.75 | 78 |
| Cu-CuO | 0.1 M KOH + 0.1 M $NO_3^-$ | 3.17 mol $h^{-1}$ $g^{-1}$ | 98.7% | −0.8 | 79 |
| Co nanosheets | 1 M KOH + 0.1 M $NO_3^-$ | 10.4 mmol $h^{-1}$ $cm^{-2}$ | 98% | −0.24 | 89 |
| Fe-cyano NSs | 1 M KOH + 0.1 M $NO_3^-$ | 42.1 mg $h^{-1}$ $cm^{-2}$ | 90% | −0.5 | 90 |
| Ni-NCNTs | 0.5 M $Na_2SO_4$ + 0.3 M $NO_3^-$ | 5.1 mg $h^{-1}$ $cm^{-2}$ | 99% | −0.5 | 92 |
| CuFe alloys | 0.1 M $Na_2SO_4$ + 100 ppm $NO_3^-$ | — | 81.1% | −0.7 | 93 |
| CuNi@C alloy | 0.1 M PBS + 50 mg $L^{-1}$ $NO_3^-$ | — | 79.6% | −1.0 | 95 |
| $Co_{0.5}Cu_{0.5}$ | 1 M KOH + 50 mM $KNO_3$ | — | 95% | −0.03 | 96 |

[a] $NH_3$ yield rate. [b] Faradaic efficiency.

attention toward the $NO_3^-RR$.[65–67] However, most metallic Cu catalysts generally convert $NO_3^-$ to $N_2$ instead of $NH_3$. In terms of an electrochemical $NH_3$ synthesis system, enhancing the $NH_3$ yield rate and selectivity of metallic Cu catalysts is critical during the reduction of $NO_3^-$. Previous literature indicated that rational structure design and crystal regulation could achieve the above-mentioned target.[68,69] For example, Fu *et al.*[70] designed Cu nanosheets as electrocatalysts for the $NO_3^-RR$, which delivered a superior catalytic activity ($NH_3$ yield rate of 390 μg $mg^{-1}$ $h^{-1}$ and FE of 99.7%) to Cu foil and Cu nanoparticles (with the yield rate being about 400 times that of Cu foil and 1.7 times that of Cu nanoparticles) (Table 3). Such excellent performance might be ascribed to the large surface areas of Cu nanosheets, which could expose abundant active sites. In a recent study, flower-like polycrystalline Cu grown *in situ* on carbon paper was fabricated by an electrodeposition technique. The unique structure provided an open reaction environment beneficial to the permeation of electrolyte, and thus enhanced the liquid-phase mass-transfer process. When regarded as a catalyst for the $NO_3^-RR$, it showed superior electrochemical activity with a large $NH_3$ formation rate of 101.4 μmol $h^{-1}$ $cm^{-2}$ and FE of 93.91% in neutral solution.

Meanwhile, an $NH_3$ yield rate of 82.4 μmol $h^{-1}$ $cm^{-2}$ was still achieved after six continuous cycles, with a high FE above 92.85% retained, indicating an alluring stability for electroreduction of $NO_3^-$ to $NH_3$.[71]

On the other hand, interface engineering, such as defect engineering,[72] heteroatom doping,[73] coupling with carbon,[65] grain-boundary engineering,[74] and constructing heterostructures[75,76] has been proposed to further enhance the electrochemical $NO_3^-RR$ activity of metallic Cu catalysts. As presented in Fig. 7a and b, Xu *et al.*[72] fabricated the atomic-defect-rich metallic Cu nanoplates (dr-Cu NPs) and investigated their catalytic activity for the $NO_3^-RR$. After the introduction of a large number of defects in the lattice, the electrochemically active surface area of the Cu nanoplates was remarkably enhanced (dr-Cu NPs: 1.28 mF $cm^{-2}$ *vs.* Cu NPs: 0.38 mF $cm^{-2}$), thus increasing the surface-active sites and facilitating the adsorption of various intermediates during the electrochemical process. As expected, dr-Cu NPs displayed a large $NO_3^-$ conversion rate of 93.26%, favorable $NH_3$ selectivity of 81.99%, as well as a high $NH_3$ FE of 85.47%, which were superior to those of Cu nanoplates without defects (Fig. 7c and d). Song *et al.*[77] designed Cu nanoparticles encapsulated in a porous carbon matrix for $NO_3^-$ to $NH_3$ conversion (Fig. 7e and f). Under an ultralow concentration of 1 mM $NO_3^-$, Cu@C delivered a high $NH_3$ FE of 72.0% and a yield rate of 469.5 μg $h^{-1}$ $cm^{-2}$ at −0.3 and −0.9 V *vs.* RHE, respectively, which were approximately 3.6 times larger than those of Cu nanoparticles (Fig. 7g and h). To reveal such impressive electrocatalytic activity, they adopted the finite-element method to simulate the enrichment effect of $NO_3^-$ on the surface of Cu@C and Cu. The structure model of a Cu slab coated with or without porous carbon shown in Fig. 7i and j suggested that the porous carbon skeleton within Cu@C was beneficial to the concentration of $NO_3^-$, thereby expediting the mass transfer of $NO_3^-$ for efficient electroreduction into $NH_3$ at ultralow concentrations. In addition, Cu nanoparticles with abundant grain boundaries encapsulated by hollow carbon (Cu@C) were constructed and regarded as an electrocatalyst for thee conversion of $NO_3^-$ to $NH_3$ in alkaline media. In terms of this catalyst system, apart from the enrichment effect of carbon, the grain boundaries within the Cu nanoparticles could appropriately regulate the adsorption energy of $NO_3^-$ for dwindling reaction barriers and enhance the reaction activity for the $NO_3^-RR$. As a consequence, the constructed Cu@C catalyst exhibited a maximum FE of 94.2% and a large $NH_3$ yield rate of 487.8 mmol $g^{-1}$ $h^{-1}$ at a low potential of −0.2 V *vs.* RHE in alkaline media, achieving an exceptional performance for the $NO_3^-RR$.[74] Zhang *et al.*[78] constructed a heterostructure catalyst composed of metallic Cu and oxygen-vacancy-rich $TiO_{2-x}$, in which the Cu nanoparticles were homogenously anchored on $TiO_{2-x}$ nanosheets (Fig. 7k). As a catalyst for the $NO_3^-RR$, the designed heterostructure electrode exhibited an $NH_3$ formation rate of 0.1143 mmol $h^{-1}$ $mg^{-1}$ along with a high FE of

Published on 02 May 2023. Downloaded on 2/6/2026 6:54:49 PM.

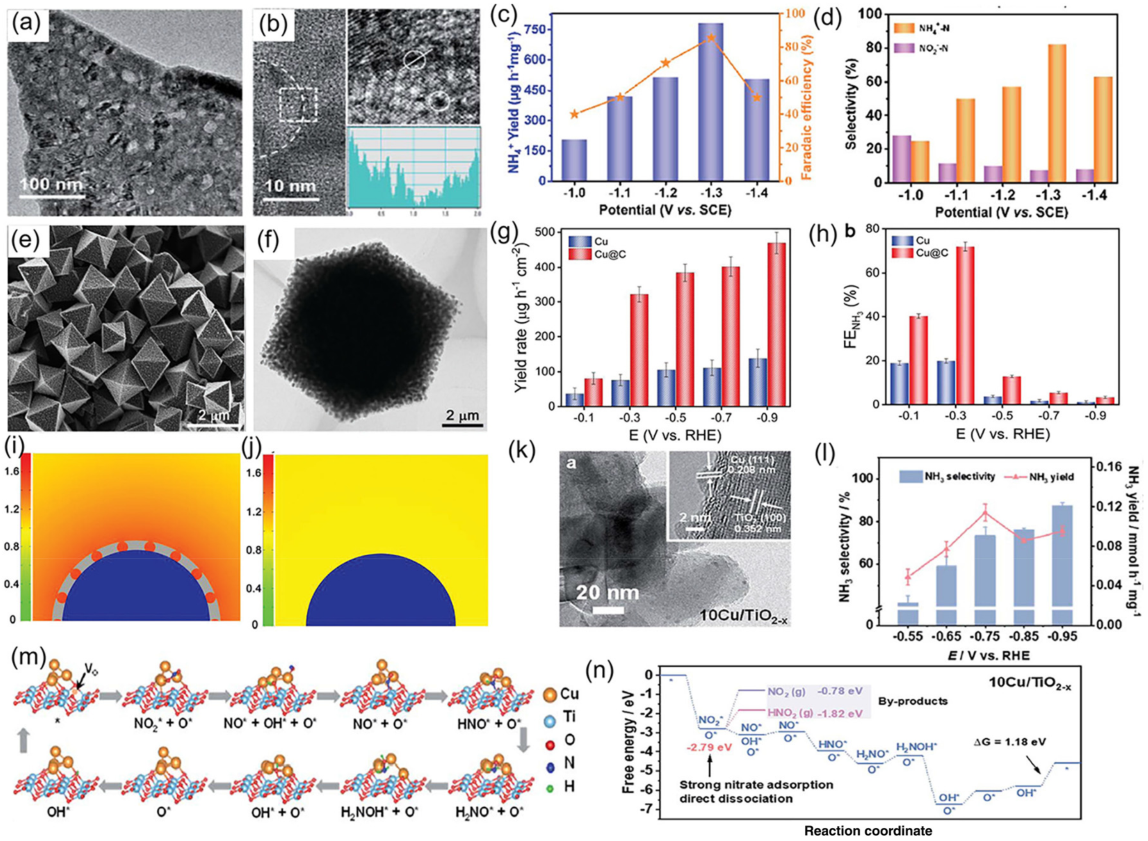

**Fig. 7** (a) TEM and (b) HRTEM images of a dr-Cu nanoplate. (c) $NH_4^+$ yield rate and FE, and (d) $NH_4^+$ selectivity of dr-Cu nanoplates at various potentials. Reproduced from ref. 72 with permission from The Royal Society of Chemistry, copyright 2021. (e) SEM and (f) TEM images of Cu@C. (g) $NH_3$ yield rate and (h) FE of Cu@C under different potentials. Simulated concentrations and distribution of local $NO_3^-$ on the surface of (i) Cu@C and (j) Cu at the diffusion time of 7 μs. The blue semicircle and the gray shell represent Cu and porous carbon, respectively. Reproduced from ref. 77 with permission from Wiley-VCH, copyright 2022. (k) TEM image of $Cu/TiO_{2-x}$. (l) $NH_3$ selectivity and yield rate of $Cu/TiO_{2-x}$ at each applied potential. (m) Reaction mechanism and (n) corresponding calculated free energy changes of the $NO_3^-$RR on the surface of $Cu/TiO_{2-x}$. Reproduced from ref. 72 with permission from The Royal Society of Chemistry, copyright 2021.

81.34%, which obviously outperformed the individual Cu and $TiO_{2-x}$ counterparts (Fig. 7l). Such excellent electrocatalytic activity could be ascribed to the introduction of oxygen defects and metallic Cu clusters, which not only modified the electronic conductivity of the heterostructure electrode, but also optimized the adsorption energy of $NO_3^-$ and hydrogenation manner that suppressed the generation of by-products (Fig. 7m and n). Similarly, Zhao *et al.*[79] designed and fabricated a Cu-CuO heterostructure as an electrocatalyst for the $NO_3^-$RR, where the heterointerface between Cu and CuO was favorable for promoting the hydrogenation of *NO to *NOH and inhibiting the HER during the reduction process of $NO_3^-$. Thus, this heterostructure catalyst showed a molar-level $NH_3$ yield rate of 3.17 mol h$^{-1}$ g$^{-1}$ and an ultrahigh FE of 98.7%. In addition, metallic Cu exhibits substantially high energy barriers to the dissociation of water in both neutral and alkaline electrolytes during electroreduction of $NO_3^-$, which controls the proton transfer rate and further leads to sluggish reaction kinetics for $NH_3$ synthesis.[80] To address the above-mentioned issue, Yu *et al.*[81] employed DFT calculations to seek applicable ligands and confirmed that the uncoordinated carboxylate ligands could considerably promote water dissociation on Cu, accelerating the proton transfer and reaction kinetics of $NO_3^-$. They experimentally encapsulated Cu nanoparticles into the uncoordinated carboxylate-ligand-rich MOF matrix through a particle decomposition route. As expected, the designed Cu-based catalyst achieved an alluring electrochemical performance for the reduction of $NO_3^-$ to $NH_3$ in alkaline media, including a high $NH_3$ yield rate of 496.4 mmol h$^{-1}$ g$^{-1}$ at an ultralow potential of −0.2 V *vs.* RHE and an outstanding stability of 20 h.

In addition to metallic Cu, other metal catalysts like Co, Fe, Ni, and Bi have been applied to highly effective reduction of $NO_3^-$ to $NH_3$.[82–87] For instance, our group synthesized metallic Co–nitrogen-doped carbon nanotubes hybrid (Co–NCNTs) (Fig. 8a and b) and investigated their electrocatalytic activity for the $NO_3^-$RR. In 0.1 M NaOH with 0.1 M $NO_3^-$, the Co–NCNTs delivered a high activity for the $NO_3^-$RR with an $NH_3$ production rate of 5996 μg h$^{-1}$ cm$^{-2}$ and FE of 92% at 0.6 V *vs.* RHE (Fig. 8c and d), and exhibited excellent durability with ~8.7% attenuation of current density and well-maintained FE during the 12-h electrolysis. Furthermore, DFT calculations

Published on 02 May 2023. Downloaded on 2/6/2026 6:54:49 PM.

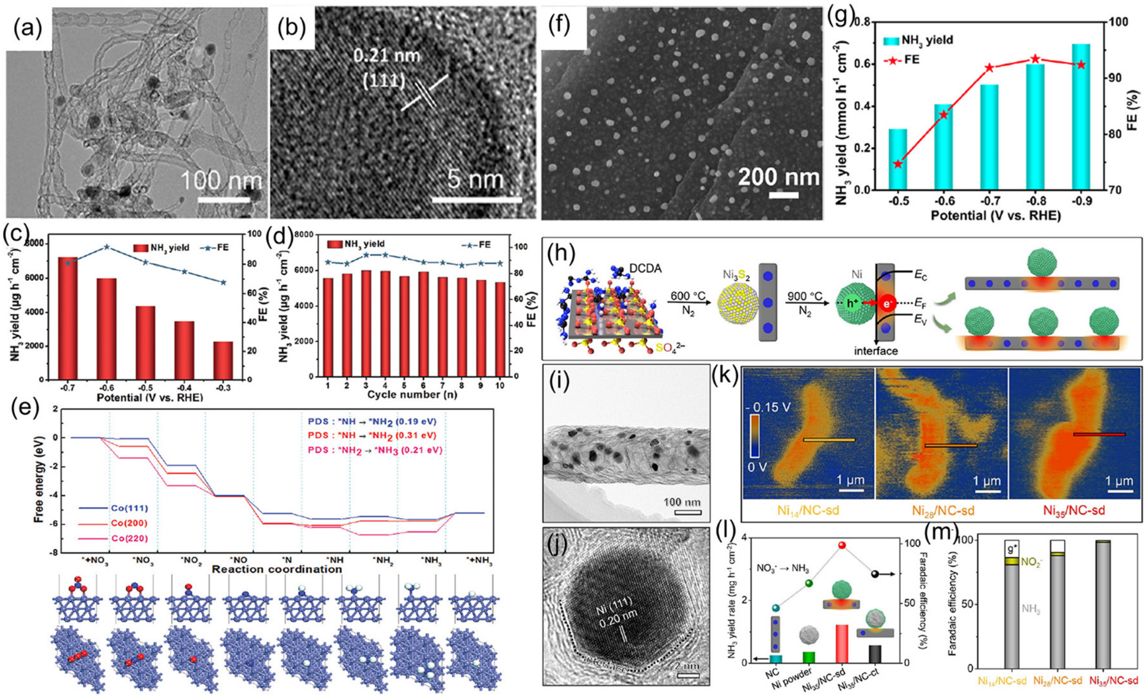

Fig. 8 (a and b) TEM images of Co-NCNTs. (c) $NH_3$ yield rate and FE of Co-NCNTs under various potentials. (d) Recycling test of Co-NCNTs at −0.6 V. (e) Free-energy profiles of the $NO_3^-RR$ on different crystal facets of metallic Co. Reproduced from ref. 88 with permission from The Royal Society of Chemistry, copyright 2022. (f) SEM image, (g) $NH_3$ yield rate and FE at different potentials of Co-carbon derived from corncob. Reproduced from ref. 89 with permission from the American Chemical Society, copyright 2022. (h) Fabrication process of Ni-NCNTs catalyst. (i and j) TEM and HRTEM images of Ni-NCNTs. (k) Surface electric field distribution of Ni-NCNTs sample. (l and m) $NH_3$ yield rate and FE of Ni-NCNTs catalyst. Reproduced from ref. 92 with permission from Wiley-VCH, copyright 2021.

(Fig. 8e) revealed that the Co (111) facet is more favorable for the $NO_3^-RR$ than the Co (200) and Co (220) facets, in which the rate-determining step is the hydrogenation of *NH to $*NH_2$. The corresponding energy barrier was only 0.19 eV, indicating the impressive $NO_3^-RR$ activity of metallic Co.[88] Meanwhile, we also synthesized metallic Co nanoparticles embedded on carbon derived from corncob as an electrocatalyst for the $NO_3^-RR$ to $NH_3$, which achieved a large $NH_3$ production rate of 0.6 mmol $h^{-1}$ $cm^2$ with a FE of 93.4%, as depicted in Fig. 8f and g.[89] Fang and coworkers[90] reported that metallic Fe anchored on cyano-coordination polymer porous nanosheets (Fe-cyano NSs) displayed an outstanding electrochemical $NH_3$ synthesis through the reduction of $NO_3^-$ in an alkaline electrolyte. Bi has also been employed as a highly efficient catalyst for electrochemical reduction of $NO_3^-$ due to its unique atomic structure, in which the interlayer lattice compression shortens the Bi–Bi bond to broaden the 6p bandwidth for electronic delocalization, enhancing the adsorption energy for nitrogen intermediates.[84] Iarchuk *et al.*[91] synthesized Ni foam catalysts through a dynamic hydrogen-bubble-template-assisted electrodeposition process. An $NH_3$ FE of more than 95% was obtained under the relatively low potential range from −0.1 to −0.3 V *vs.* RHE. Gao *et al.*[92] constructed a Schottky heterostructure composed of metallic Ni and nitrogen-doped carbon nanotubes (Ni-NCNTs) for converting $NO_3^-$ to $NH_3$ at room temperature (Fig. 8h–j). In terms of heterostructure catalyst, the heterointerface between Ni nanoparticles and NCNTs could induce the formation of a built-in electric field (Fig. 8k), which facilitated the accumulation and fixation of $NO_3^-$ on the surface of the catalyst and consequently promoting the reaction kinetics during the electrochemical process. As a result, the designed Ni-NCNTs enabled a high FE of 99% for the electrocatalytic reduction of $NO_3^-$, and a large $NH_3$ formation rate of 5.1 mg $h^{-1}$ $cm^{-2}$ in the electrochemical conversion of $NO_3^-$ (Fig. 8l and m).

**3.3.2 Metal alloys.** Coupling with a secondary metal has been regarded as a fascinating route to enhance the electrochemical activity of transition-metal catalysts *via* regulating the electronic structure of the metal and exerting a synergistic effect of two different metals. Table 3 summarizes the electrochemical performance of metal alloy catalysts for the $NO_3^-RR$. For instance, Tang *et al.*[93] demonstrated that Cu–Fe bimetallic nanoalloys with a Cu/Fe molar ratio of 3 : 1 presented a high $NH_3$ FE of 81.1% at −0.7 V *vs.* RHE within 6 h in 0.1 M $Na_2SO_4$ containing 100 ppm $NO_3^-$. Similarly, Sargent and coauthors[94] indicated that $Cu_{50}Ni_{50}$ alloy catalysts only required an overpotential of 0.2 V to obtain the maximum $NH_3$ FE under various concentrations of $NO_3^-$, and produced a 6-times increment in the $NO_3^-RR$ activity compared to the case of pure Cu at 0 V *vs.* RHE. DFT calculations revealed that the introduction of Ni atoms led to the upshifting of the d-band center toward the Fermi level, which improved the adsorption energies of the

Published on 02 May 2023. Downloaded on 2/6/2026 6:54:49 PM.

intermediates and enhanced the selectivity for $NH_3$. Recently, Liu *et al.*[95] incorporated CuNi alloy nanoparticles into a nitrogen-doped carbon matrix with hierarchical pores by pyrolysis of bimetallic MOFs. A high $NH_3$ selectivity of 94.4% and FE of 79.6% were achieved when utilizing the designed CuNi@C as a catalyst for the $NO_3^-$RR. Jeon *et al.*[96] designed cobalt–copper ($Co_{1-x}Cu_x$) nanoparticles supported on a three-dimensional substrate for efficient and selective $NH_3$ synthesis *via* an electrocatalytic $NO_3^-$ reduction. Typically, the optimized $Co_{0.5}Cu_{0.5}$ catalyst performed at a high $NH_3$ FE of over 95% at −0.03 V with an $NH_3$ partial current density of ∼176 mA $cm^{-2}$ at 50 mM nitrate, which is 7.3- and 1.7-fold higher than those of the pure Co and Cu counterparts, respectively. Importantly, replacing Co with Cu enabled tuning of the onset potential on the Co catalyst and maintained a high selectivity toward $NH_3$.

## 3.4 Transition-metal compound catalysts

### 3.4.1 Metal oxides

*3.4.1.1 Copper-based oxides.* Transition-metal oxides have been widely investigated as electrocatalysts for $NH_3$ synthesis *via* converting $NO_3^-$ under ambient conditions (Table 4). As summarized in the above section, metallic Cu has been intensively studied for the electroreduction of $NO_3^-$ to $NH_3$ owing to its favorable adsorption ability for $NO_3^-$ and various intermediates (*e.g.*, $NO_2^-$ and NO). However, pure Cu catalysts still suffer from serious catalytic instability. For the purpose of overcoming this issue, substantial efforts have recently been made into the study of Cu-based oxide catalysts for highly-efficient electrochemical $NO_3^-$ to $NH_3$ conversion.

For example, Yuan *et al.*[97] explored the influence of Cu oxidation state on the electrochemical reduction of $NO_3^-$, and found that the $NH_3$ formation rate and FE of a Cu electrode could be significantly boosted after surface oxidation. After that, Ren *et al.*[98] designed and fabricated core–shell structural $Cu@Cu_{2+1}O$ nanowires (Fig. 9a–c) for electrochemical conversion of $NO_3^-$ to $NH_3$. In terms of the $Cu@Cu_{2+1}O$ catalyst, the interior metallic Cu components could provide pathways for fast electron transfer due to the one-dimensional nanowire structure, while the exterior $Cu_{2+1}O$ layer affords a massive amount of catalytically active sites. Furthermore, DFT calculation results suggested that the introduction of a surface oxidation layer regulated the Cu d-band center and modulated the adsorption energies of various intermediates. Therefore, the constructed $Cu@Cu_{2+1}O$ catalyst exhibited a high $NH_3$ yield rate of 576.53 μg $h^{-1}$ $mg^{-1}$ associated with a FE of 87.7% at −0.564 V *vs.* RHE, and $NH_3$ selectivity of 76% (Fig. 9d). Qin *et al.*[99] further illustrated the effects of the surface structure of $Cu_2O$ (exposing facets) on $NO_3^-$ reduction to $NH_3$. Both experimental and theoretical calculation results illustrated that the $Cu_2O$ (100) facet featured a relatively smaller energy barrier for $NH_3$ formation than the $Cu_2O$ (111) facet, leading to a large $NH_3$ formation rate (743 μg $h^{-1}$ $mg^{-1}$) and high FE (82.3%) at −0.6 V *vs.* RHE.

Table 4 Summary of catalytic performance of transition-metal compound electrocatalysts

| Catalyst | Electrolyte | $NH_3$ yield rate | Faradaic efficiency | Potentials (V *vs.* RHE) | Ref. |
|---|---|---|---|---|---|
| $Cu@Cu_{2+1}O$ nanowires | 0.5 M $K_2SO_4$ + 50 mg $L^{-1}$ $NO_3^-$ | 576.53 μg $h^{-1}$ $mg^{-1}$ | 87.7% | −0.545 | 98 |
| $CuO@MnO_2$ | 0.5 M $K_2SO_4$ + 100 mg $L^{-1}$ $NO_3^-$ | 0.240 mmol $h^{-1}$ $cm^{-2}$ | 94.92% | −0.645 | 104 |
| $CuO_x/TiO_2$ | 0.5 M $Na_2SO_4$ + 100 ppm $NO_3^-$ | 1241.81 μg $h^{-1}$ $cm^{-2}$ | 92.34% | −0.75 | 105 |
| $TiO_{2-x}$ nanotubes | 0.5 M $Na_2SO_4$ + 50 ppm $NO_3^-$ | 0.045 mmol $h^{-1}$ $mg^{-1}$ | 85% | −0.945 | 109 |
| Co-doped $TiO_2$ nanosheet | 0.1 M NaOH + 0.1 M $NO_3^-$ | 1127 μmol $h^{-1}$ $cm^{-2}$ | 98.2% | $-0.9^a/-0.5^b$ | 111 |
| $Co@TiO_2$ | 0.1 M PBS + 0.1 M $NO_3^-$ | 800 μmol $h^{-1}$ $cm^{-2}$ | 96.7% | $-1.0^a/-0.7^b$ | 112 |
| $FeS_2@TiO_2$ | 0.1 M NaOH + 0.1 M $NaNO_3$ | 860.3 μmol $h^{-1}$ $cm^{-2}$ | 97.0% | $-0.7^a/-0.4^b$ | 114 |
| Cu-doped $Co_3O_4$ nanowire | 0.1 M $Na_2SO_4$ + 500 ppm $NO_3^-$ | 36.71 mmol $h^{-1}$ $g^{-1}$ | 86.5% | −0.6 | 117 |
| $Co_3O_4$ nanosheets with Co vacancies | 0.1 M NaOH + 0.1 M $NaNO_3$ | 517.5 μmol $h^{-1}$ $cm^{-2}$ | 97.2% | $-0.6^a/-0.4^b$ | 118 |
| $NiCo_2O_4$ nanowire | 0.1 M KOH + 0.1 M $NaNO_3$ | 973.2 μmol $h^{-1}$ $cm^{-2}$ | 99.0% | $-0.6^a/-0.3^b$ | 121 |
| $ZnCo_2O_4$ nanoarray | 0.1 M KOH + 0.1 M $NaNO_3$ | 634.74 mmol $h^{-1}$ $cm^{-2}$ | 98.33% | $-0.8^a/-0.6^b$ | 122 |
| BCDs/$NiCo_2O_4$ nanowire | 0.5 M $K_2SO_4$ + 200 ppm $NO_3^-$ | 173.9 μmol $h^{-1}$ $cm^{-2}$ | 100% | −0.55 | 124 |
| $CuO@Co_3O_4$ | 1 M KOH + 1400 ppm $NO_3^-$ | 1.915 mmol $h^{-1}$ $cm^{-2}$ | 99.17% | −0.23 | 125 |
| Co-doped $Fe/Fe_2O_3$ | 0.1 M $Na_2SO_4$ + 50 ppm $NO_3^-$ | 1505.9 μg $h^{-1}$ $cm^{-2}$ | 85.2% | −0.95 | 135 |
| $CoTiO_{3-x}$ nanofibers | 0.1 M NaOH + 0.1 M $NaNO_3$ | 30.4 mg $h^{-1}$ $mg_{cat}^{-1}$ | 92.6% | $-1.1^a/-1.0^b$ | 136 |
| $CuWO_4$ nanospheres | 0.5 M $Na_2SO_4$ + 0.05 M $NaNO_3$ | 5.84 mg $h^{-1}$ $mg^{-1}$ | 94.6% | −0.7 | 137 |
| $Cu_3P$ nanowires | 0.1 M PBS + 0.1 M $NaNO_3$ | 1626.6 ± 36.1 μg $h^{-1}$ $cm^{-2}$ | 91.2 ± 2.5% | −0.5 | 141 |
| CoP nanosheets | 1.0 M NaOH + 1.0 M $NaNO_3$ | 9.56 mol $h^{-1}$ $m^{-2}$ | 100% | −0.3 | 143 |
| $Bi_2S_3/MoS_2$ | 0.1 M $Na_2SO_4$ + 0.1 M $NaNO_3$ | $15.04 \times 10^{-2}$ mmol $h^{-1}$ $cm^{-2}$ | 88.4% | −0.8 | 146 |
| $Ni_3N$ nanoparticles | 0.5 M $Na_2SO_4$ + 0.5 M $NaNO_3$ | 9.185 mmol $h^{-1}$ $mg^{-1}$ | 89.5% | −0.795 | 148 |
| $Fe_3C$ nanoflakes | 1 M KOH + 75 mM $KNO_3$ | 1.19 mmol $h^{-1}$ $mg^{-1}$ | 96.7% | −0.5 | 150 |

[a] $NH_3$ yield rate. [b] Faradaic efficiency.

Published on 02 May 2023. Downloaded on 2/6/2026 6:54:49 PM.

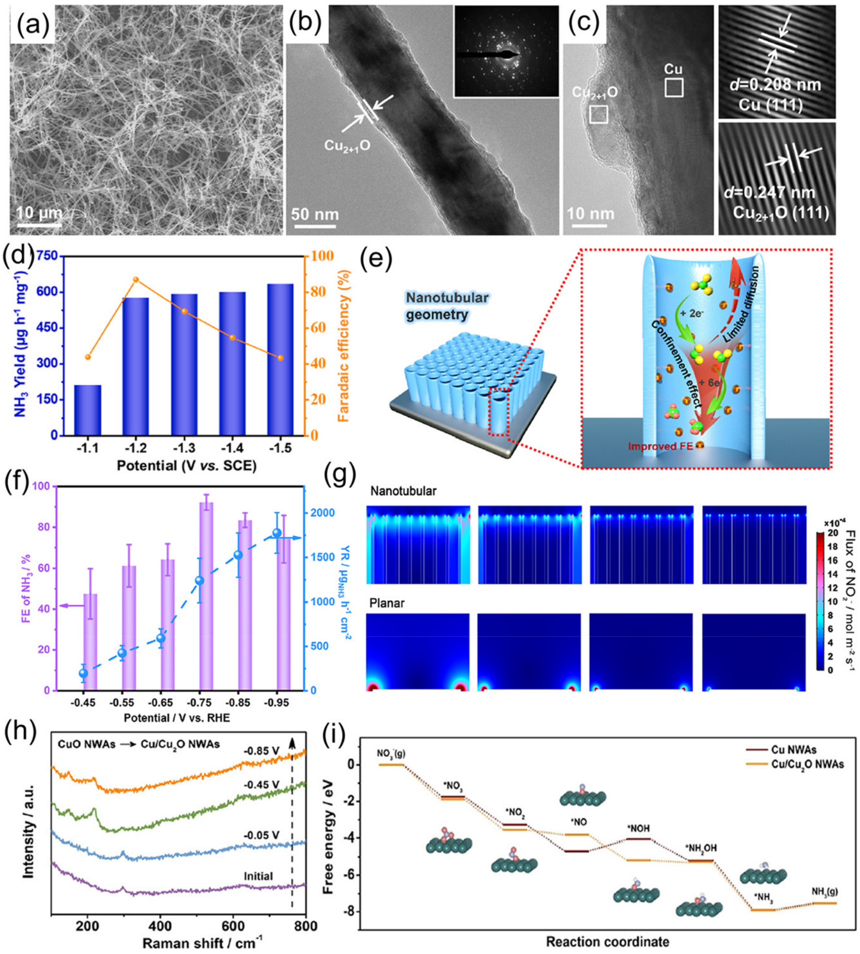

**Fig. 9** (a) SEM, (b) TEM and (c) HRTEM images of Cu@$Cu_{2+1}O$ nanowires. (d) $NH_3$ formation rate and FE of Cu@$Cu_{2+1}O$ nanowires under the applied potentials. Reproduced from ref. 98 with permission from Elsevier, copyright 2021. (e) Schematic illustration of $NO_3^-$-to-$NH_3$ reduction over electrodes with nanotubular geometries. (f) $NH_3$ FE and yield rate of $CuO_x/TiO_2$ at varying potentials. (g) Simulated $NO_2^-$ concentration distribution on nanotubular and planar geometries. Reproduced from ref. 105 with permission from Elsevier, copyright 2022. (h) *In situ* electrochemical Raman spectra of CuO nanowires at given potentials. (i) Free-energy diagram for the $NO_3^-$RR over Cu nanowires. Reproduced from ref. 106 with permission from Wiley-VCH, copyright 2020.

To further enhance the electrocatalytic activity of $Cu_2O$ toward the $NO_3^-$RR, various strategies have been employed, such as introducing oxygen defects[100,101] and constructing heterostructures.[79,102,103] For example, Xu *et al.*[104] designed core–shell structural CuO@$MnO_2$ hierarchical nanoarrays grown on Cu foam (CuO@$MnO_2$/CF) for the $NO_3^-$RR. The heterointerface between the CuO nanowires and $MnO_2$ nanosheets enabled abundant catalytically active sites and induced the formation of a built-in electric field, which were beneficial to the capture of $NO_3^-$ and various intermediates during the electrochemical reactions, as well as accelerate ionic/electronic transfer at the interface. With these properties, CuO@$MnO_2$/CF achieved an impressive electrochemical performance including a very-high $NO_3^-$ conversion of 99.38%, $NH_3$ FE of 94.92%, and selectivity of 96.67%. Meanwhile, this catalyst exhibits excellent stability, maintaining the $NH_3$ yield rate and FE after 5 consecutive recycling tests. Qiu *et al.*[105] incorporated $CuO_x$ nanoparticles into a $TiO_2$-nanotube reactor for highly selective conversion of $NO_3^-$ to $NH_3$. In this $CuO_x/TiO_2$ catalyst system, $TiO_2$ nanotubes could efficiently hinder the diffusion of $NO_2^-$ intermediate and promote the conversion of $NO_3^-$ to $NH_3$ (Fig. 9e and g). The constructed $CuO_x/TiO_2$ heterostructure achieved a yield rate of 1241.81 μg $h^{-1}$ $cm^{-2}$, a high FE of 92.93% (Fig. 9f), and outstanding durability with a stable FE during the ten successive cycles of electrolysis.

Cu-based oxidation catalysts present outstanding electrochemical activity toward selective reduction of $NO_3^-$ to $NH_3$, but the origin of their activity and the structural evolution that occurs during the electrochemical reaction process were still experimentally unclear. In this regard, Zhang and his co-workers applied *in situ* characterization techniques to unveil the active phase of the CuO electrocatalyst. Experimental results suggested that CuO was transformed to Cu/$Cu_2O$ during the reduction process of $NO_3^-$, and served as an active phase for $NO_3^-$ conversion (Fig. 9h). Then, online differential electrochemical mass spectrometry was adopted to analyze the

Published on 02 May 2023. Downloaded on 2/6/2026 6:54:49 PM.

reaction pathway. $NO_3^-$ adsorbed on the surface of electrode was firstly reduced to $*NO_2$ and *NO, in which *NO was hydrogenated to give *NHON and $*NH_2OH$. Subsequently, $*NH_2OH$ was converted to $*NH_3$ and further desorbed from the surface of the electrode generating $NH_3$. DFT calculations also discovered that the origin of the activity enhancement was attributed to the reconstructed structure, in which electron transfer from $Cu_2O$ to Cu at the interface could promote the generation of the *NOH intermediate and limit the competing HER (Fig. 9i).[106]

*3.4.1.2 Titanium-based oxides.* Titanium oxide ($TiO_2$) is a promising electrocatalyst candidate for the electrochemical reduction of $NO_3^-$ owing to its advantages in terms of cost and robustness.[107,108] For example, Jia *et al.*[109] fabricated $TiO_2$ nanotubes rich in oxygen vacancies as an electrocatalyst for the $NO_3^-RR$. An outstanding conversion rate of 95.2% for $NH_3$ production from $NO_3^-$ electroreduction associated with a FE of 85% was achieved. DFT calculations revealed that $NO_3^-$ was adsorbed on the surface of the electrode and preferentially filled the oxygen defects existing in the $TiO_2$ nanotubes, which weakened the N–O bonding, modulated the adsorption energies of the intermediates, and limited the generation of by-products. Analogously, oxygen-vacancy-$TiO_2$ nanomaterials composed of rutile and anatase phases were fabricated as a catalyst for $NH_3$ synthesis from the electroreduction of $NO_3^-$, which could deliver an $NH_3$ FE of 78.0% and selectivity of 81.9%. Online differential electrochemical mass spectrometry and first-principle calculations revealed that the existence of oxygen vacancies ($Ti^{3+}$) and the heterointerface between the rutile and anatase phases were favorable for modulating the adsorption energy of $NO_3^-$ and facilitating the hydrogenation reaction to form *NOH, which led to a relatively high $NH_3$ selectivity and FE.[110] However, the limited selectivity for $NH_3$ and sluggish reaction kinetics hinder their further application for $NH_3$ electrosynthesis.

In this regard, our group proposed a series of modification strategies for improving the above-mentioned issues, such as heteroatom doping, and constructing Schottky junctions and p–n heterojunctions. For example, taking a Co-based catalyst with high catalytic activity into consideration, we introduced Co heteroatoms into a $TiO_2$ nanoribbon array supported on Ti foil for electroreduction of $NO_3^-$ (Fig. 10a and b). Co-doping can effectively improve the intrinsic electronic conductivity of $TiO_2$ and increase the content of oxygen defects in $TiO_2$, which further facilitates the adsorption of $NO_3^-$ and transportation of charge at the interface, as well as decreasing the energy barrier of the potential-determining step (Fig. 10c). As a result, Co-doped $TiO_2$ nanoribbon arrays delivered a large $NH_3$ production rate of 1127 μmol $h^{-1}$ $cm^{-2}$ and a high FE of 98.2%, which was remarkably superior to that of its counterpart in alkaline media (88.5 μmol $h^{-1}$ $cm^{-2}$; 35.1%), as presented in Fig. 10d and e.[111] Inspired by this, we further constructed a Schottky junction by integrating metallic Co nanoparticles into $TiO_2$ nanobelt arrays ($Co@TiO_2$) (Fig. 10f and g). A built-in electric field formed at the heterointerface between Co and $TiO_2$, which was beneficial for the capture of $NO_3^-$ on the

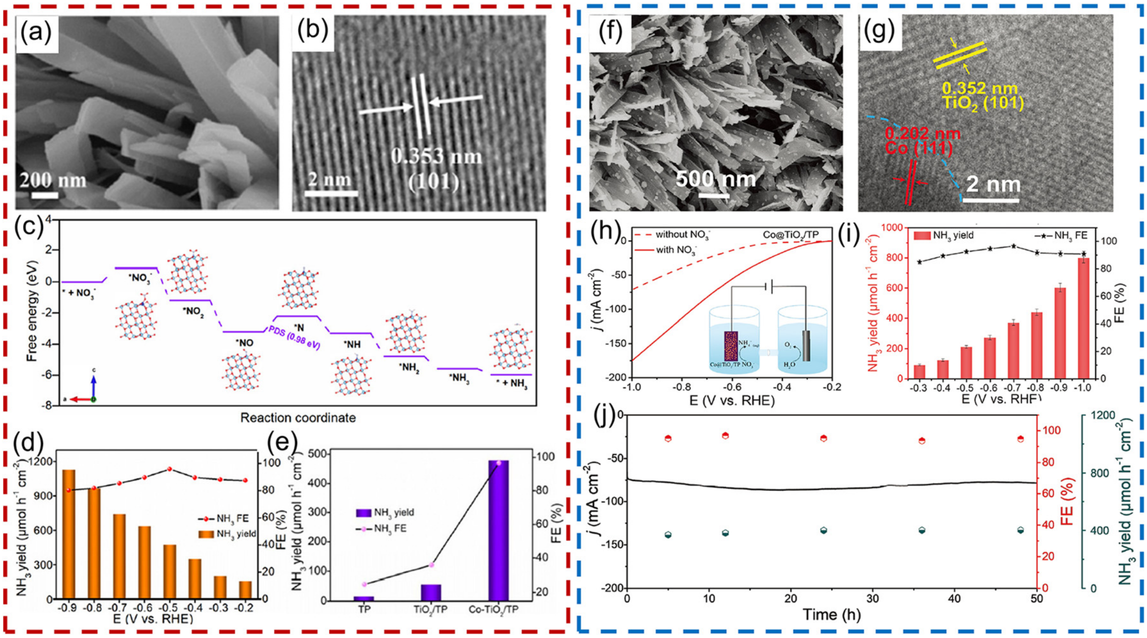

**Fig. 10** (a) SEM and (b) HRTEM images of Co-doped $TiO_2$. (c) Calculated free-energy changes of the $NO_3^-RR$ on the Co-doped $TiO_2$. (d) $NH_3$ yield rate and FE of Co-doped $TiO_2$ under given potentials. (e) Comparison of $NH_3$ yield rate and FE between $TiO_2$ and Co-doped $TiO_2$. Reproduced from ref. 111 with permission from The Royal Society of Chemistry, copyright 2022. (f) SEM and (g) HRTEM images of $Co@TiO_2$ heterojunction catalyst. (h) LSV curves and (i) $NH_3$ formation rate and FE at given potentials for $Co@TiO_2$. (j) The long-term electrocatalytic performance of the $Co@TiO_2$ catalyst. Reproduced from ref. 112 with permission from Wiley-VCH, copyright 2023.

Published on 02 May 2023. Downloaded on 2/6/2026 6:54:49 PM.

surface of the electrocatalyst and thus facilitated mass transfer during the electroreduction process of $NO_3^-$. Consequently, in a neutral medium containing 0.1 M $NO_3^-$, the as-designed Co@$TiO_2$ catalyst enabled a high $NH_3$ FE of 96.7% at −0.7 V *vs.* RHE and a competitive $NH_3$ formation rate of 800 μmol $h^{-1}$ $cm^{-2}$ at −1.0 V (Fig. 10h and i). Meanwhile, this catalyst also showed impressive durability during recycling tests and 50 h of bulk electrolysis (Fig. 10j).[112] Following this, $Fe_3O_4$@$TiO_2$,[113] CoP@$TiO_2$ [114] and $FeS_2$@$TiO_2$ [115] p–n heterojunctions were constructed by our team and utilized as electrocatalysts to convert $NO_3^-$ to $NH_3$, where the selectivity and efficiency of bare $TiO_2$ for the $NO_3^-$RR were significantly enhanced.

*3.4.1.3 Spinel oxide.* Spinel-type oxides feature unique advantages in terms of versatility, flexible ion arrangement, multivalence structure, and superior electronic conductivity, making them promising electrocatalysts for the $NO_3^-$RR.[116] For example, $Co_3O_4$ has been extensively utilized as a catalyst for the electroreduction of $NO_3^-$, but its yield rate and selectivity of the target product $NH_3$ are relatively low.[117] To enhance the electrocatalytic activity of $Co_3O_4$, our group[118] designed $Co_3O_4$ nanosheet arrays with Co vacancies on carbon cloth for converting $NO_3^-$ to $NH_3$ (Fig. 11a and b). As presented in Fig. 11c and d, $Co_3O_4$ with Co vacancies delivered a high $NH_3$ yield rate of 517.5 μmol $h^{-1}$ $g^{-1}$ and a maximum FE of 97.2% at −0.6 and −0.4 V *vs.* RHE in alkaline electrolyte, respectively, which were higher than those of bare $Co_3O_4$ nanosheets (183.8 μmol $h^{-1}$ $g^{-1}$ with a FE of 85.9%). Furthermore, DFT calculations demonstrated that the introduction of Co vacancies regulated the electron structure of $Co_3O_4$, optimized the adsorption energy of $NO_3^-$ and reduced the energy barrier of the potential-determining step (*NHO to *NHOH), leading to the high electrocatalytic activity (Fig. 11e and f). Similarly, we adopted Fe as a dopant to modulate the electron structure of $Co_3O_4$, further elevating its selectivity and $NH_3$ yield rate during the electroreduction of $NO_3^-$.[119] In line with the above-mentioned viewpoint, many bimetal spinel oxides, such as $FeCo_2O_4$,[120] $NiCo_2O_4$,[121] $ZnCo_2O_4$,[122] $AlCo_2O_4$,[77] and $NiFe_2O_4$,[123] have been synthesized and investigated as electrocatalysts for a highly efficient $NO_3^-$RR by our team. As demonstrated in Fig. 11g and h, $NiCo_2O_4$ nanowire arrays grown on carbon cloth were synthesized for electrochemical $NH_3$ production by conversion of $NO_3^-$. Owing to the synergistic effects of the two metal sites, $NiCo_2O_4$ nanowire arrays attained a large $NH_3$ formation rate of 973.2 μmol $h^{-1}$ $cm^{-2}$ and large FE of 99.0% (Fig. 11i and j) in 0.1 M KOH with 0.1 M $NaNO_3$.

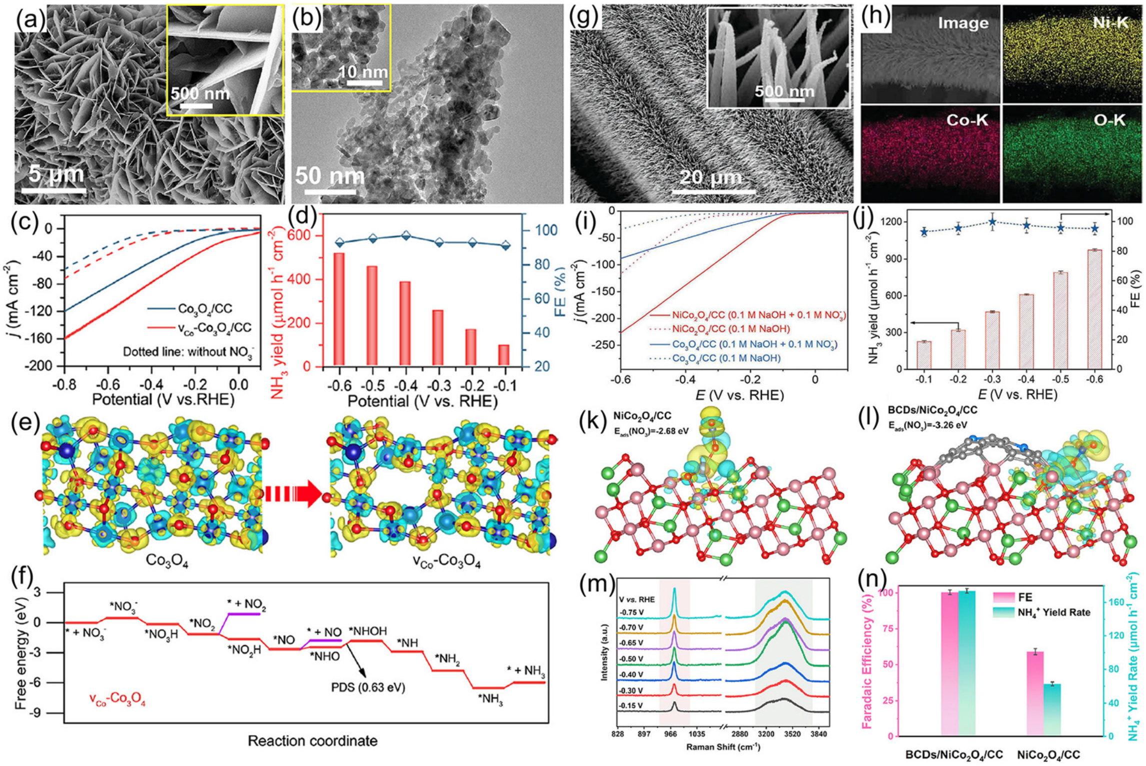

**Fig. 11** (a) SEM and (b) TEM images of $Co_3O_4$ nanosheets with Co vacancies. (c) LSV curves and (d) $NH_3$ yield rate, FE under different potentials for $Co_3O_4$ nanosheets with Co vacancies. (e) Charge density distribution of $Co_3O_4$ with/without Co vacancies. (f) Free-energy diagrams for the $NO_3^-$RR on $Co_3O_4$ with Co vacancies. Reproduced from ref. 118 with permission from the American Chemical Society, copyright 2022. (g and h) SEM and mapping images of $NiCo_2O_4$. (i) LSV curves and (j) yield rate and FE of $NH_3$ under given potentials. Reproduced from ref. 121 with permission from the Wiley-VCH, copyright 2022. Charge-density difference for $NO_3^-$ adsorption on $NiCo_2O_4$ (k) and BCDs/$NiCo_2O_4$ (l). (m) *In situ* Raman spectra of $NO_3^-$RR over BCDs/$NiCo_2O_4$ at different applied potentials. (n) Comparison of $NH_3$ FEs and yield rate of BCDs/$NiCo_2O_4$ and $NiCo_2O_4$. Reproduced from ref. 124 with permission from the Elsevier, copyright 2022.

Published on 02 May 2023. Downloaded on 2/6/2026 6:54:49 PM.

Impressively, the as-designed $NiCo_2O_4$ nanowires displayed exceptional durability with no significant fluctuations in both $NH_3$ production rate and FE after 16 successive electrolysis experiments. After that, taking the Lewis-base property of $NO_3^-$ into consideration, Lu *et al.*[124] further introduced abundant Lewis acid sites on the surface of $NiCo_2O_4$ nanowire arrays for increasing the adsorption energy of $NO_3^-$ by coupling with boron-doped carbon dots (BCDs/$NiCo_2O_4$). As revealed in Fig. 11k and l, the incorporation of BCDs enhanced the adsorption energy of $NO_3^-$ on the surface of the BCDs/$NiCo_2O_4$ electrode. Meanwhile, *in situ* Raman spectra shown in Fig. 11m suggested that the intensity of the peak at 975 $cm^{-1}$ associated with the N–O stretching vibration was boosted under the applied potentials, indicating that the Lewis acid sites induced by BCD doping were critically important for enhancing the adsorption ability of $NO_3^-$. As expected, the BCDs/$NiCo_2O_4$ catalyst provided a nearly ~100% FE and a large $NH_3$ production rate of 173.9 μmol $h^{-1}$ $cm^{-2}$ at −0.55 V *vs.* RHE (Fig. 11n).

$Co_3O_4$ as an electrocatalyst for the $NO_3^-RR$ still suffers from the critical issue that it is difficult to electrochemically reduce $NO_3^-$ to $NO_2^-$ using this catalyst. As mentioned above, Cu-based materials possess excellent electrocatalytic activity for $NO_3^-$ to $NO_2^-$, and thus constructing a $Co_3O_4$-based heterostructure with Cu-based materials could achieve promising electrochemical performance. Liu *et al.*[125] fabricated $Co_3O_4$ grown on CuO nanowire arrays to construct a hierarchical heterostructure for an efficient $NO_3^-RR$. At −0.23 V *vs.* RHE, CuO@$Co_3O_4$ provided an $NH_3$ yield rate of 1.915 mmol $h^{-1}$ $cm^{-2}$, which was higher than those of CuO and $Co_3O_4$. Fu *et al.*[126] built dual active sites on a $Co_3O_4$/Cu electrode, in which Cu focused on the reduction of $NO_3^-$ to $NO_2^-$, and then $Co_3O_4$ generated H* (active hydrogen) as a strong reducing agent to further convert $NO_2^-$ to $NH_3$. As a result, the $Co_3O_4$/Cu catalyst presented a large $NH_3$ yield rate of 684 μg $mg^{-1}$ $h^{-1}$ with 94.6% FE. Recently, Fan *et al.*[127] fabricated a $Co_3O_4$ nanosheet grown *in situ* on $TiO_2$ nanosheet arrays for the $NO_3^-RR$, which gave a large $NH_3$ yield rate of 875 μmol $mg^{-1}$ $h^{-1}$ and a high FE of 93.1% in alkaline electrolyte.

*3.4.1.4 Other metal oxides.* Other types of transition-metal oxides have also been investigated for the $NO_3^-RR$, such as $Bi_2O_3$, $Mn_3O_4$, $BiFeO_3$, and $La_2CuO_4$.[128–131] However, the inferior electronic conductivity of metal oxides hinders their electrocatalytic activity. Currently, regulating their electronic structure through oxygen-defect engineering is a promising strategy.[132,133] For instance, Wang *et al.*[134] fabricated ultrathin $CoO_x$ nanosheets with abundant surface oxygen as an $NO_3^-RR$ catalyst, attaining a large $NH_3$ yield of 82.4 ± 4.8 mg $h^{-1}$ $mg^{-1}$ with a FE of 93.4 ± 3.8% at −0.3 V *vs.* RHE. The surface oxygen on the Co sites was prone to stabilize the adsorbed hydrogen on $CoO_x$, and thus efficiently suppressed the formation of $H_2$ and achieved a high selectivity for $NH_3$ synthesis. Zhang *et al.*[135] reported a Co-doped Fe/$Fe_2O_3$ catalyst for electrochemical $NH_3$ synthesis by reducing $NO_3^-$ under ambient conditions. This catalyst afforded an $NH_3$ production rate of 1505.9 μg $h^{-1}$ $cm^{-2}$ with a FE of 85.2% and a high $NH_3$ selectivity of 99.0%. Recently, our group reported that $CoTiO_{3-x}$ nanofibers with oxygen vacancies showed an $NH_3$ formation rate of 30.4 mg $h^{-1}$ $mg^{-1}$ and a large FE of 92.6% in 0.1 M NaOH solution containing 0.1 M $NO_3^-$.[136] The $CuWO_4$ hollow nanospheres with oxygen vacancies showed a high $NH_3$ FE of 94.6% and yield rate of 5.84 mg $h^{-1}$ $mg^{-1}$ at −0.7 V *vs.* RHE.[137]

**3.4.2 Metal phosphides.** Metal phosphides featuring metallic characteristics and high catalytic activities for the HER have become fascinating electrocatalysts for converting $NO_3^-$ to $NH_3$, which is attributed to the fact that they can afford hydrogen at a small overpotential during the electroreduction process. So far, many transition-metal phosphides, such as CoP, $Ni_2P$, and $Cu_3P$, have been used as catalysts for $NH_3$ electrosynthesis.[138–142] For example, Ye *et al.*[143] reported that CoP nanosheet arrays supported on carbon cloth exhibited a molar level $NH_3$ formation rate of 9.56 mol $h^{-1}$ $m^{-2}$ at −0.3 V *vs.* RHE with a FE of ~100% under alkaline conditions (Fig. 12a–c). Furthermore, the reaction mechanism of the $NO_3^-RR$ on the surface of CoP was investigated by coupling *in situ* characterization technology and theoretical calculations (Fig. 12d and e). As presented in Fig. 12f, Co 4p orbitals directly participated in the adsorption of $NO_3^-$ *via* Co–O–N bonds and the electron-transfer step of the $NO_3^-RR$, while phosphorus within CoP could stabilize the active phase and reduce the reaction-energy barrier of the rate-determining step during the electroreduction of $NO_3^-$, thus leading to a highly selective electrosynthesis of $NH_3$ from $NO_3^-$. $Ni_2P$ nanoparticles supported on Ni foam were synthesized and regarded as an electrocatalyst for electrochemically converting $NO_3^-$ to $NH_3$ in neutral media with 50 mM $NO_3^-$. A high $NH_3$ evolving rate of 0.056 mmol $h^{-1}$ $cm^{-2}$ with a FE of 99.23%, and a selectivity of 89.1% were obtained.[144] As shown in Fig. 12g, our group[141] synthesized $Cu_3P$ nanowire arrays anchored on copper foam for electrochemical conversion of $NO_3^-$ to $NH_3$ in neutral media. In 0.1 M phosphate-buffered saline (PBS) containing 0.1 M $NaNO_3$, a $Cu_3P$ nanowire catalyst delivered a large $NH_3$ formation rate of 848.7 ± 18.0 μg $h^{-1}$ $cm^{-2}$ and a high FE of 62.9 ± 2.0% at −0.6 V *vs.* RHE (Fig. 12h and i).

**3.4.3 Other metal compounds.** Recently, other metal compounds have also been applied as electrocatalysts for $NO_3^-$ to $NH_3$ conversion at room temperature.[145–147] Zhang *et al.*[148] fabricated $Ni_3N$ nanoparticles embedded on a carbon skeleton and investigated its electrochemical performance as a catalyst for the $NO_3^-RR$. This catalyst provided a high $NH_3$ selectivity of 89.5% and large yield rate of 9.185 mmol $h^{-1}$ $mg^{-1}$ at −0.795 V *vs.* RHE in neutral media. Amorphous $CoB_x$ nanoparticles anchored on carbon paper were synthesized *via* a simple wet chemical reduction method. When used for electroreduction of $NO_3^-$ to $NH_3$, $CoB_x$ afforded a maximum FE of 94.0% and a yield rate of up to 0.787 mmol $h^{-1}$ $cm^{-2}$.[149] Wang *et al.*[150] reported that $Fe_3C$ nanoflakes embedded on N-doped carbon nanosheets displayed an $NH_3$ yield rate of 1.19 mmol $h^{-1}$ $mg^{-1}$, $NH_3$ FE of 96.7%, and selectivity of 79.0% at −0.5 V *vs.* RHE.

Published on 02 May 2023. Downloaded on 2/6/2026 6:54:49 PM.

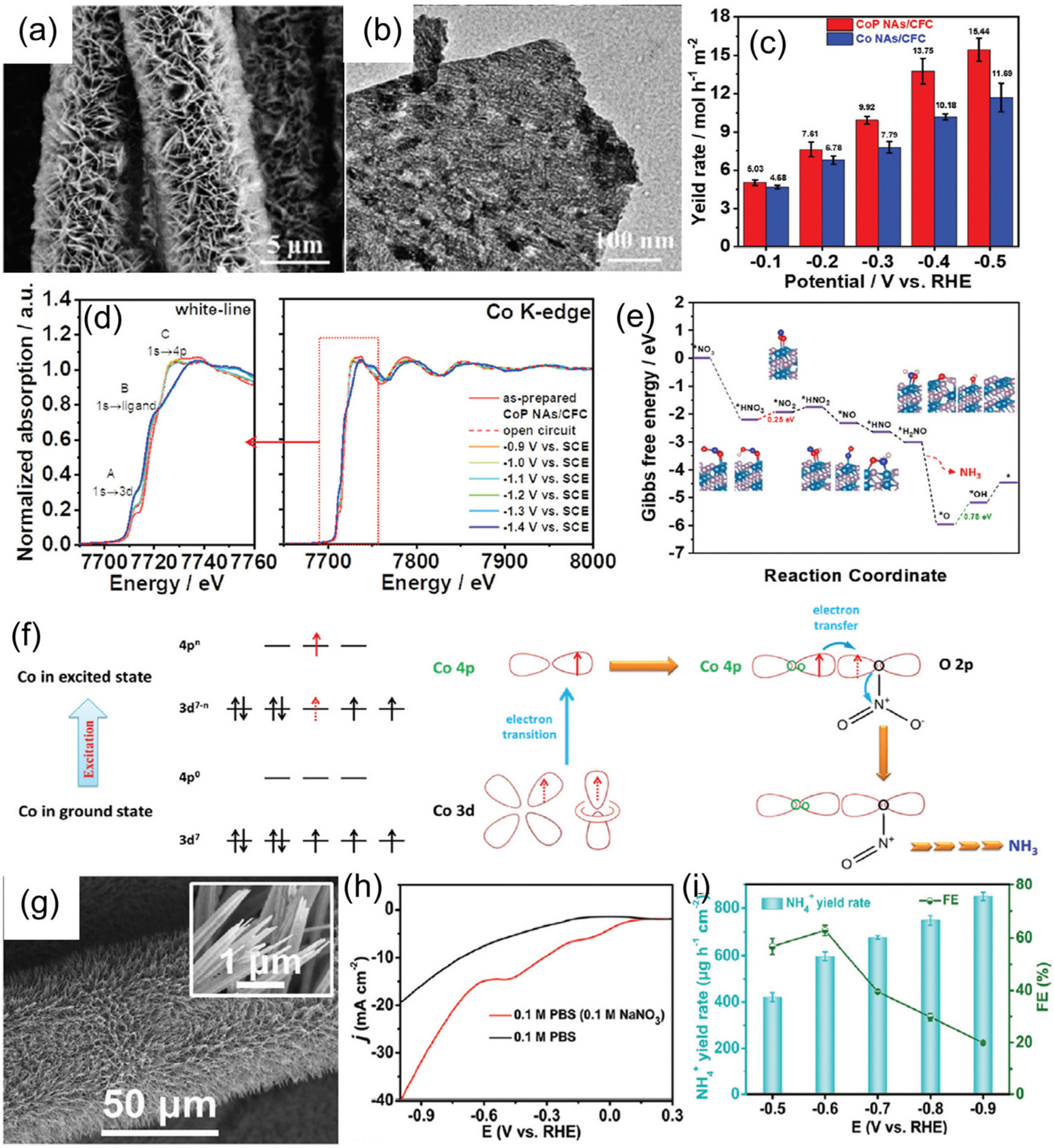

**Fig. 12** (a) SEM and (b) TEM images of CoP. (c) $NH_3$ yield rate of CoP at given potentials. (d) *In situ* XANES of the Co K-edge of CoP. (e) Gibbs free-energy diagram of the $NO_3^-RR$ on CoP. (f) Mechanism of the $NO_3^-RR$ on CoP. Reproduced from ref. 143 with permission from The Royal Society of Chemistry, copyright 2022. (g) SEM image of $Cu_3P$. (h) LSV curve, (i) $NH_3$ yield rate and FE of $Cu_3P$ in $NaNO_3$. Reproduced from ref. 141 with permission from The Royal Society of Chemistry, copyright 2021.

## 4. Conclusions

The electrochemical $NO_3^-RR$ has opened up a green and sustainable route for $NH_3$ synthesis under ambient conditions, which is associated with two advantages: (i) the electrochemical $NH_3$ synthesis from $NO_3^-$ utilizes water as a proton source and is powered by renewable energy, which means that this process avoids the utilization of fossil fuels and reduces the $NH_3$ production cost; (ii) the benign reaction conditions of the conversion of $NO_3^-$ would enable distributed $NH_3$ production in smaller-scale devices, which facilitates the production of fertilizer on demand and realizes a neutral carbon footprint. The important electrochemical characteristics of $NH_3$ yield rate, Faradaic efficiency and selectivity largely depend on the electrocatalysts. Therefore, this review briefly describes the electroreduction mechanism from $NO_3^-$ to $NH_3$ under mild environmental conditions and summarizes the recent development of various electrocatalysts including noble-metal-based materials, single-atom metal catalysts, and transition-metal-based materials. Meanwhile,

Published on 02 May 2023. Downloaded on 2/6/2026 6:54:49 PM.

various effective design strategies for enhancing the electrocatalytic activity are outlined. Furthermore, it provides profound insights into the knowledge behind various optimization strategies, which are imperative for the development of highly-efficient electrocatalysts for the electrochemical conversion of $NO_3^-$ to $NH_3$. Although considerable progress has been achieved so far, the following points should also be considered in this field:

(i) As mentioned in the discussion above, ongoing research into electrochemical $NH_3$ synthesis from $NO_3^-$ mainly focuses on the design and investigation of metal-based materials; less attention has been given to the exploration of metal-free electrocatalysts. From the energy-saving and emission-reduction points of view, it is of great significance to explore metal-free electrocatalysts with high activity, large selectivity and excellent stability for enabling the electrocatalytic $NO_3^-$RR under ambient conditions. As a consequence, more attention should be given to elaborately developing carbon-based electrocatalysts for the $NO_3^-$RR, providing an alluring strategy for large-scale $NH_3$ production.

(ii) The electrochemical $NO_3^-$RR, as an emerging strategy for $NH_3$ production under ambient conditions, has attained a dramatic growth in interest and various catalysts have been investigated in this field. However, none of the suitable catalysts can be regarded as a benchmark catalyst for electrocatalytic $NO_3^-$RR research. Besides, the variety of experimental details, such as the pH value of the electrolyte and the concentration of the nitrogen resource, play a critical role in catalytic activity and selectivity, and their effects on the electrochemical performance remain to be thoroughly studied. Such issues lead to incomparable results and thus limit the mutual communication and promotion in the community. Therefore, finding a standard catalyst and unification of experimental parameters are urgently required in the field of the electrochemical $NO_3^-$RR.

(iii) Many catalysts have exhibited superior catalytic activity and high $NH_3$ selectivity during the electrochemical $NO_3^-$RR process, but their catalytic mechanisms and reaction processes were only revealed by theoretical calculations and remain unclear experimentally. For this reason, *in situ* characterization to scrutinize the pristine catalyst surface evolution (surface structure, element valence state, and exposed active sites) and adsorbed intermediates should be elaborately developed to uncover the real catalytic sites and reaction pathways upon the electrochemical reaction process for the rational design of electrocatalysts for the $NO_3^-$RR.

(iv) From the point of view of practical application, besides the fact that the electrochemical $NO_3^-$RR to $NH_3$ process is still developing and lacks a catalyst with excellent durability and performance for supporting long-term electrolysis at the moment, another challenge is that this process will generate a tremendous amount of $H_2$ as a side-product during the electrolysis, which is directly vented off into the atmosphere, forming a safety issue. Therefore, tremendous efforts are required before the electrochemical $NO_3^-$RR to $NH_3$ can be put into practical operation.

## Conflicts of interest

There are no conflicts to declare.

## Acknowledgements

The authors extend their appreciation to the Deanship of Scientific Research at King Khalid University for funding support through large group Research Project under Grant No. RGP2/199/44.

## References

1 S. L. Foster, S. I. P. Bakovic, R. D. Duda, S. Maheshwari, R. D. Milton, S. D. Minteer, M. J. Janik, J. N. Renner and L. F. Greenlee, Catalysts for nitrogen reduction to ammonia, *Nat. Catal.*, 2018, **1**, 490–500.

2 Y. C. Wan, J. C. Xu and R. T. Lv, Heterogeneous electrocatalysts design for nitrogen reduction reaction under ambient conditions, *Mater. Today*, 2019, **27**, 69–90.

3 J. Liang, Q. Liu, A. A. Alshehri and X. Sun, Recent advances in nanostructured heterogeneous catalysts for N-cycle electrocatalysis, *Nano Res. Energy*, 2022, **1**, e9120010.

4 J. W. S. Erisman, M. A. Sutton, J. Galloway, Z. Klimont and W. Winiwarter, How a century of ammonia synthesis changed the world. W, *Nat. Geosci.*, 2008, **1**, 636–639.

5 R. Schlogl, Catalytic synthesis of ammonia—A "never-ending story"?, *Angew. Chem., Int. Ed.*, 2003, **42**, 2004–2008.

6 C. Philibert, Renewable energy for industry: from green energy to green materials and fuels, IEA Report, 2017.

7 J. G. Chen, R. M. Crooks, L. C. Seefeldt, K. L. Bren, R. M. Bullock, M. Y. Darensbourg, P. L. Holland, B. Hoffman, M. J. Janik, A. K. Jones, M. G. Kanatzidis, P. King, K. M. Lancaster, S. V. Lymar, P. Pfromm, W. F. Schneider and R. R. Schrock, Beyond fossil fuel–driven nitrogen transformations, *Science*, 2018, **360**, eaar6611.

8 L. Wang, M. Xia, H. Wang, K. Huang, C. Qian, C. T. Maravelias and G. A. Ozin, Greening ammonia toward the solar ammonia refinery, *Joule*, 2018, **2**, 1055–1074.

9 B. Ma, H. Zhao, T. Li, Q. Liu, Y. Luo, C. Li, S. Lu, A. M. Asiri, D. Ma and X. Sun, Iron-group electrocatalysts for ambient nitrogen reduction reaction in aqueous media, *Nano Res.*, 2021, **14**, 555–569.

10 X. Zhu, S. Mou, Q. Peng, Q. Liu, Y. Luo, G. Chen, S. Gao and X. Sun, Aqueous electrocatalytic $N_2$ reduction for ambient $NH_3$ synthesis: recent advances in catalyst development and performance improvement, *J. Mater. Chem. A*, 2020, **8**, 1545–1556.

This journal is © the Partner Organisations 2023

Published on 02 May 2023. Downloaded on 2/6/2026 6:54:49 PM.

11 C. Tang and S. Z. Qiao, How to explore ambient electrocatalytic nitrogen reduction reliably and insightfully, *Chem. Soc. Rev.*, 2019, **48**, 3166–3180.

12 T. Xu, B. Ma, J. Liang, L. Yue, Q. Liu, T. Li, H. Zhao, Y. Luo, S. Lu and X. Sun, Recent progress in metal-free electrocatalysts toward ambient $N_2$ reduction reaction, *Acta Phys.–Chim. Sin.*, 2021, **37**, 2009043.

13 Q. Liu, T. Xu, Y. Luo, Q. Kong, T. Li, S. Lu, A. A. Alshehri, K. A. Alzahrani and X. Sun, Recent advances in strategies for highly selective electrocatalytic $N_2$ reduction toward ambient $NH_3$ synthesis, *Curr. Opin. Electrochem.*, 2021, **29**, 100766.

14 D. Liu, M. Chen, X. Du, H. Ai, K. H. Lo, S. Wang, S. Chen, G. Xing, X. Wang and H. Pan, Development of electrocatalysts for efficient nitrogen reduction reaction under ambient condition, *Adv. Funct. Mater.*, 2021, **31**, 2008983.

15 P. H. van Langevelde, I. Katsounaros and M. T. M. Koper, Electrocatalytic nitrate reduction for sustainable ammonia production, *Joule*, 2021, **5**, 290–294.

16 Y. Xu, K. Shi, T. Ren, H. Yu, K. Deng, X. Wang, H. Wang and L. Wang, Electronic metal-support interaction triggering interfacial charge polarization over CuPd/N-doped-C nanohybrids drives selectively electrocatalytic conversion of nitrate to ammonia, *Small*, 2022, **18**, 2203335.

17 Y. Wang, C. Wang, M. Li, Y. Yu and B. Zhang, Nitrate electroreduction: mechanism insight, in situ characterization, performance evaluation, and challenges, *Chem. Soc. Rev.*, 2021, **50**, 6720–6733.

18 D. Anastasiadou, Y. van Beek, E. J. M. Hensen and M. C. Figueiredo, Ammonia electrocatalytic synthesis from nitrate, *Electrochem. Sci. Adv.*, 2022, DOI: **10.1002/elsa.202100220**.

19 J. Theerthagiri, J. Park, H. T. Das, N. Rahamathulla, E. S. F. Cardoso, A. P. Murthy, G. Maia, D. V. N. Vo and M. Y. Choi, Electrocatalytic conversion of nitrate waste into ammonia: a review, *Environ. Chem. Lett.*, 2022, **20**, 2929–2949.

20 H. Xu, Y. Ma, J. Chen, W. X. Zhang and J. Yang, Electrocatalytic reduction of nitrate–A step towards a sustainable nitrogen cycle, *Chem. Soc. Rev.*, 2022, **51**, 2710.

21 Z. Li, Z. Deng, L. Ouyang, X. Fan, L. Zhang, S. Sun, Q. Liu, A. A. Alshehri, Y. Luo, Q. Kong and X. Sun, $CeO_2$ nanoparticles with oxygen vacancies decorated N-doped carbon nanorods: A highly efficient catalyst for nitrate electroreduction to ammonia, *Nano Res.*, 2022, **15**, 8914–8921.

22 Q. Liu, Q. Liu, L. Xie, L. Yue, T. Li, Y. Luo, N. Li, B. Tang, L. Yu and X. Sun, A 3D FeOOH nanotube array: an efficient catalyst for ammonia electrosynthesis by nitrite reduction, *Chem. Commun.*, 2022, **58**, 5160–5163.

23 Y. Arikawa, Y. Otsubo, H. Fujino, S. Horiuchi, E. Sakuda and K. Umakoshi, Nitrite reduction cycle on a dinuclear ruthenium complex producing ammonia, *J. Am. Chem. Soc.*, 2018, **140**, 842–847.

24 H. Chen, C. Zhang, L. Sheng, M. Wang, W. Fu, S. Gao, Z. Zhang, S. Chen, R. Si, L. Wang and B. Yang, Copper single-atom catalyst as a high-performance electrocatalyst for nitrate-ammonium conversion, *J. Hazard. Mater.*, 2022, **434**, 128892.

25 Y. Zeng, C. Priest, G. Wang and G. Wu, Restoring the nitrogen cycle by electrochemical reduction of nitrate: progress and prospects, *Small Methods*, 2020, **4**, 2000672.

26 X. Zhang, Y. Wang, C. Liu, Y. Yu, S. Lu and B. Zhang, Recent advances in non-noble metal electrocatalysts for nitrate reduction, *Chem. Eng. J.*, 2021, **403**, 126269.

27 S. Garcia-Segura, M. Lanzarini-Lopes, K. Hristovski and P. Westerhoff, Electrocatalytic reduction of nitrate: Fundamentals to full-scale water treatment applications, *Appl. Catal., B*, 2018, **236**, 546–568.

28 M. D. V. Rosca, M. T. de Groot and M. T. M. Koper, Nitrogen cycle electrocatalysis, *Chem. Rev.*, 2009, **109**, 2209–2244.

29 M. T. de Groot and M. T. M. Koper, The influence of nitrate concentration and acidity on the electrocatalytic reduction of nitrate on platinum, *J. Electroanal. Chem.*, 2004, **562**, 81–94.

30 R. Lange, E. Maisonhaute, R. Robin and V. Vivier, On the kinetics of the nitrate reduction in concentrated nitric acid, *Electrochem. Commun.*, 2013, **29**, 25–28.

31 D. Sicsic, F. Balbaud-Célérier and B. Tribollet, Mechanism of nitric acid reduction and kinetic modelling, *Eur. J. Inorg. Chem.*, 2014, **2014**, 6174–6184.

32 D. Xu, Y. Li, L. Yin, Y. Ji, J. Niu and Y. Yu, Electrochemical removal of nitrate in industrial wastewater, *Front. Environ. Sci. Eng.*, 2018, **12**, 9.

33 J. Gao, B. Jiang, C. Ni, Y. Qi and X. Bi, Enhanced reduction of nitrate by noble metal-free electrocatalysis on P doped three-dimensional $Co_3O_4$ cathode: Mechanism exploration from both experimental and DFT studies, *Chem. Eng. J.*, 2020, **382**, 123034.

34 A. C. A. de Vooys, R. A. van Santen and J. A. R. van Veen, Electrocatalytic reduction of $NO_3^-$ onpalladium/copper electrodes, *J. Mol. Catal. A: Chem.*, 2000, **154**, 203–215.

35 W. L. M. D. Bartberger, E. Ford, K. M. Miranda, C. Switzer, J. M. Fukuto, P. J. Farmer, D. A. Wink and K. N. Houk, The reduction potential of nitric oxide (NO) and its importance to NO biochemistry, *Proc. Natl. Acad. Sci. U. S. A.*, 2002, **99**, 10958.

36 A. C. A. de Vooys, M. T. M. Koper, R. A. van Santen and J. A. R. van Veen, Mechanistic study of the nitric oxide reduction on a polycrystalline platinum electrode, *Electrochim. Acta*, 2001, **46**, 923–930.

37 T. Yoshioka, K. Iwase, S. Nakanishi, K. Hashimoto and K. Kamiya, Electrocatalytic reduction of nitrate to nitrous oxide by a copper-modified covalent triazine framework, *J. Phys. Chem. C*, 2016, **120**, 15729–15734.

38 G. A. Cerrón-Calle, A. S. Fajardo, C. M. Sánchez-Sánchez and S. Garcia-Segura, Highly reactive Cu-Pt bimetallic 3D-electrocatalyst for selective nitrate reduction to ammonia, *Appl. Catal., B*, 2022, **302**, 120844.

39 C. A. Clark, C. P. Reddy, H. Xu, K. N. Heck, G. Luo, T. P. Senftle and M. S. Wong, Mechanistic insights into

Published on 02 May 2023. Downloaded on 2/6/2026 6:54:49 PM.

pH-controlled nitrite reduction to ammonia and hydrazine over rhodium, *ACS Catal.*, 2020, **10**, 494–509.

40 X. Li, X. Zhao, Y. Zhou, J. Hu, H. Zhang, X. Hu and G. Hu, Pd nanocrystals embedded in $BC_2N$ for efficient electrochemical conversion of nitrate to ammonia, *Appl. Surf. Sci.*, 2022, **584**, 152556.

41 M. Jiang, A. Tao, Y. Hu, L. Wang, K. Zhang, X. Song, W. Yan, Z. Tie and Z. Jin, Crystalline modulation engineering of Ru nanoclusters for boosting ammonia electrosynthesis from dinitrogen or nitrate, *ACS Appl. Mater. Interfaces*, 2022, **14**, 17470–17478.

42 J. Li, G. Zhan, J. Yang, F. Quan, C. Mao, Y. Liu, B. Wang, F. Lei, L. Li, A. W. M. Chan, L. Xu, Y. Shi, Y. Du, W. Hao, P. K. Wong, J. Wang, S. X. Dou, L. Zhang and J. C. Yu, Efficient ammonia electrosynthesis from nitrate on strained ruthenium nanoclusters, *J. Am. Chem. Soc.*, 2020, **142**, 7036–7046.

43 J. Lim, C. Y. Liu, J. Park, Y. H. Liu, T. P. Senftle, S. W. Lee and M. C. Hatzell, Structure sensitivity of Pd facets for enhanced electrochemical nitrate reduction to ammonia, *ACS Catal.*, 2021, **11**, 7568–7577.

44 T. Ren, Z. Yu, H. Yu, K. Deng, Z. Wang, X. Li, H. Wang, L. Wang and Y. Xu, Interfacial polarization in metal-organic framework reconstructed Cu/Pd/$CuO_x$ multi-phase heterostructures for electrocatalytic nitrate reduction to ammonia, *Appl. Catal., B*, 2022, **318**, 121805.

45 Y. Xu, K. Ren, T. Ren, M. Wang, Z. Wang, X. Li, L. Wang and H. Wang, Ultralow-content Pd in-situ incorporation mediated hierarchical defects in corner-etched $Cu_2O$ octahedra for enhanced electrocatalytic nitrate reduction to ammonia, *Appl. Catal., B*, 2022, **306**, 121094.

46 M. Liu, Q. Mao, K. Shi, Z. Wang, Y. Xu, X. Li, L. Wang and H. Wang, Electroreduction of nitrate to ammonia on palladium–cobalt–oxygen nanowire arrays, *ACS Appl. Mater. Interfaces*, 2022, **14**, 13169–13176.

47 Y. Xu, K. Ren, T. Ren, M. Wang, M. Liu, Z. Wang, X. Li, L. Wang and H. Wang, Cooperativity of Cu and Pd active sites in CuPd aerogels enhances nitrate electroreduction to ammonia, *Chem. Commun.*, 2021, **57**, 7525–7528.

48 Q. Gao, H. S. Pillai, Y. Huang, S. Liu, Q. Mu, X. Han, Z. Yan, H. Zhou, Q. He, H. Xin and H. Zhu, Breaking adsorption-energy scaling limitations of electrocatalytic nitrate reduction on intermetallic CuPd nanocubes by machine-learned insights, *Nat. Commun.*, 2022, **13**, 2338.

49 G. Zhang, X. Li, P. Shen, Y. Luo, X. Li and K. Chu, PdNi nanosheets boost nitrate electroreduction to ammonia, *J. Environ. Chem. Eng.*, 2022, **10**, 108362.

50 Y. Xu, Y. Sheng, M. Wang, T. Liu, H. Yu, K. Deng, Z. Wang, L. Wang and H. Wang, Lattice-strain and Lewis acid sites synergistically promoted nitrate electroreduction to ammonia over PdBP nanothorn arrays, *J. Mater. Chem. A*, 2022, **10**, 16290–16296.

51 H. Liu, J. Park, Y. Chen, Y. Qiu, Y. Cheng, K. Srivastava, S. Gu, B. H. Shanks, L. T. Roling and W. Li, Electrocatalytic nitrate reduction on oxide-derived silver with tunable selectivity to nitrite and ammonia, *ACS Catal.*, 2021, **11**, 8431–8442.

52 J. Qin, K. Wu, L. Chen, X. Wang, Q. Zhao, B. Liu and Z. Ye, Achieving high selectivity for nitrate electrochemical reduction to ammonia over MOF-supported $Ru_xO_y$ clusters, *J. Mater. Chem. A*, 2022, **10**, 3963–3969.

53 Y. Wang, H. Li, W. Zhou, X. Zhang, B. Zhang and Y. Yu, Structurally disordered $RuO_2$ nanosheets with rich oxygen vacancies for enhanced nitrate electroreduction to ammonia, *Angew. Chem., Int. Ed.*, 2022, **61**, e202202604.

54 H. Niu, Z. Zhang, X. Wang, X. Wan, C. Shao and Y. Guo, Theoretical insights into the mechanism of selective nitrate-to-ammonia electroreduction on single-atom catalysts, *Adv. Funct. Mater.*, 2021, **31**, 2008533.

55 L. Lv, Y. Shen, J. Liu, X. Meng, X. Gao, M. Zhou, Y. Zhang, D. Gong, Y. Zheng and Z. Zhou, Computational screening of high activity and selectivity TM/$gC_3N_4$ single-atom catalysts for electrocatalytic reduction of nitrates to ammonia, *J. Phys. Chem. Lett.*, 2021, **12**, 11143–11150.

56 T. Zhu, Q. Chen, P. Liao, W. Duan, S. Liang, Z. Yan and C. Feng, Single-atom Cu catalysts for enhanced electrocatalytic nitrate reduction with significant alleviation of nitrite production, *Small*, 2020, **16**, 2004526.

57 J. Li, Y. Zhang, C. Liu, L. Zheng, E. Petit, K. Qi, Y. Zhang, H. Wu, W. Wang, A. Tiberj, X. Wang, M. Chhowalla, L. Lajaunie, R. Yu and D. Voiry, 3.4% Solar-to-ammonia efficiency from nitrate using Fe single atomic catalyst supported on $MoS_2$ nanosheets, *Adv. Funct. Mater.*, 2022, **32**, 2108316.

58 Z. Y. Wu, M. Karamad, X. Yong, Q. Huang, D. A. Cullen, P. Zhu, C. Xia, Q. Xiao, M. Shakouri, F. Y. Chen, J. Y. T. Kim, Y. Xia, K. Heck, Y. Hu, M. S. Wong, Q. Li, I. Gates, S. Siahrostami and H. Wang, Electrochemical ammonia synthesis via nitrate reduction on Fe single atom catalyst, *Nat. Commun.*, 2021, **12**, 2870.

59 P. Li, Z. Jin, Z. Fang and G. Yu, A single-site iron catalyst with preoccupied active centers that achieves selective ammonia electrosynthesis from nitrate, *Energy Environ. Sci.*, 2021, **14**, 3522–3531.

60 J. Yang, H. Qi, A. Li, X. Liu, X. Yang, S. Zhang, Q. Zhao, Q. Jiang, Y. Su, L. Zhang, J. F. Li, Z. Q. Tian, W. Liu, A. Wang and T. Zhang, Potential-driven restructuring of Cu single atoms to nanoparticles for boosting the electrochemical reduction of nitrate to ammonia, *J. Am. Chem. Soc.*, 2022, **144**, 12062–12071.

61 X. F. Cheng, J. H. He, H. Q. Ji, H. Y. Zhang, Q. Cao, W. J. Sun, C. L. Yan and J. M. Lu, Coordination symmetry breaking of single-atom catalysts for robust and efficient nitrate electroreduction to ammonia, *Adv. Mater.*, 2022, **34**, 2205767.

62 W. D. Zhang, H. Dong, L. Zhou, H. Xu, H. R. Wang, X. Yan, Y. Jiang, J. Zhang and Z. G. Gu, Fe single-atom catalysts with pre-organized coordination structure for efficient electrochemical nitrate reduction to ammonia, *Appl. Catal., B*, 2022, **317**, 121750.

This journal is © the Partner Organisations 2023

Published on 02 May 2023. Downloaded on 2/6/2026 6:54:49 PM.

63 J. Cai, Y. Wei, A. Cao, J. Huang, Z. Jiang, S. Lu and S. Q. Zang, Electrocatalytic nitrate-to-ammonia conversion with ~100% Faradaic efficiency via single-atom alloying, *Appl. Catal., B*, 2022, **316**, 121683.

64 E. Murphy, Y. Liu, I. Matanovic, S. Guo, P. Tieu, Y. Huang, A. Ly, S. Das, I. Zenyuk, X. Pan, E. Spoerke and P. Atanassov, Highly durable and selective Fe- and Mo-based atomically dispersed electrocatalysts for nitrate reduction to ammonia via distinct and synergized $NO_2^-$ pathways, *ACS Catal.*, 2022, **12**, 6651–6662.

65 D. Yin, Y. Liu, P. Song, P. Chen, X. Liu, L. Cai and L. Zhang, In situ growth of copper/reduced graphene oxide on graphite surfaces for the electrocatalytic reduction of nitrate, *Electrochim. Acta*, 2019, **324**, 134846.

66 G. F. Chen, Y. Yuan, H. Jiang, S. Y. Ren, L. X. Ding, L. Ma, T. Wu, J. Lu and H. Wang, Electrochemical reduction of nitrate to ammonia via direct eight-electron transfer using a copper–molecular solid catalyst, *Nat. Energy*, 2020, **5**, 605–613.

67 E. Pérez-Gallent, M. C. Figueiredo, I. Katsounaros and M. T. M. Koper, Electrocatalytic reduction of nitrate on copper single crystals in acidic and alkaline solutions, *Electrochim. Acta*, 2017, **227**, 77–84.

68 X. Wang, M. Zhu, G. Zeng, X. Liu, C. Fang and C. Li, A three-dimensional Cu nanobelt cathode for highly efficient electrocatalytic nitrate reduction, *Nanoscale*, 2020, **12**, 9385–9391.

69 K. Wu, C. Sun, Z. Wang, Q. Song, X. Bai, X. Yu, Q. Li, Z. Wang, H. Zhang, J. Zhang, X. Tong, Y. Liang, A. Khosla and Z. Zhao, Surface reconstruction on uniform Cu nanodisks boosted electrochemical nitrate reduction to ammonia, *ACS Mater. Lett.*, 2022, **4**, 650–656.

70 X. Fu, X. Zhao, X. Hu, K. He, Y. Yu, T. Li, Q. Tu, X. Qian, Q. Yue, M. R. Wasielewski and Y. Kang, Alternative route for electrochemical ammonia synthesis by reduction of nitrate on copper nanosheets, *Appl. Mater. Today*, 2020, **19**, 100620.

71 Y. Zhao, Y. Liu, Z. Zhang, Z. Mo, C. Wang and S. Gao, Flower-like open-structured polycrystalline copper with synergistic multi-crystal plane for efficient electrocatalytic reduction of nitrate to ammonia, *Nano Energy*, 2022, **97**, 107124.

72 Y. Xu, M. Wang, K. Ren, T. Ren, M. Liu, Z. Wang, X. Li, L. Wang and H. Wang, Atomic defects in pothole-rich two-dimensional copper nanoplates triggering enhanced electrocatalytic selective nitrate-to-ammonia transformation, *J. Mater. Chem. A*, 2021, **9**, 16411–16417.

73 L. Yang, J. Li, F. Du, J. Gao, H. Liu, S. Huang, H. Zhang, C. Li and C. Guo, Interface engineering cerium-doped copper nanocrystal for efficient electrochemical nitrate-to-ammonia production, *Electrochim. Acta*, 2022, **411**, 140095.

74 Q. Hu, Y. Qin, X. Wang, H. Zheng, K. Gao, H. Yang, P. Zhang, M. Shao and C. He, Grain boundaries engineering of hollow copper nanoparticles enables highly efficient ammonia electrosynthesis from nitrate, *CCS Chem.*, 2022, **4**, 2053–2064.

75 X. Zhao, G. Hu, F. Tan, S. Zhang, X. Wang, X. Hu, A. V. Kuklin, G. V. Baryshnikov, H. Ågren, X. Zhou and H. Zhang, Copper confined in vesicle-like BCN cavities promotes electrochemical reduction of nitrate to ammonia in water, *J. Mater. Chem. A*, 2021, **9**, 23675–23686.

76 X. Zhu, H. Huang, H. Zhang, Y. Zhang, P. Shi, K. Qu, S. B. Cheng, A. L. Wang and Q. Lu, Filling mesopores of conductive metal–organic frameworks with Cu clusters for selective nitrate reduction to ammonia, *ACS Appl. Mater. Interfaces*, 2022, **14**, 32176–32182.

77 Z. Song, Y. Liu, Y. Zhong, Q. Guo, J. Zeng and Z. Geng, Efficient Electroreduction of Nitrate into Ammonia at Ultralow Concentrations Via an Enrichment Effect, *Adv. Mater.*, 2022, **34**, 2204306.

78 X. Zhang, C. Wang, Y. Guo, B. Zhang, Y. Wang and Y. Yu, Cu clusters/$TiO_{2-x}$ with abundant oxygen vacancies for enhanced electrocatalytic nitrate reduction to ammonia, *J. Mater. Chem. A*, 2022, **10**, 6448–6453.

79 J. Zhao, Z. Shen, J. Yu, Y. Guo, M. Mushtaq, Y. Ding, Z. Song, W. Zhang, X. Huang, Y. Li, D. Liu and X. Cai, Constructing Cu-CuO heterostructured skin on Cu cubes to promote electrocatalytic ammonia production from nitrate wastewater, *J. Hazard Mater.*, 2022, **439**, 129653.

80 M. Luo, Z. Wang, Y. C. Li, J. Li, F. Li, Y. Lum, D. H. Nam, B. Chen, J. Wicks, A. Xu, T. Zhuang, W. R. Leow, X. Wang, C. T. Dinh, Y. Wang, Y. Wang, D. Sinton and E. H. Sargent, Hydroxide promotes carbon dioxide electroreduction to ethanol on copper via tuning of adsorbed hydrogen, *Nat. Commun.*, 2019, **10**, 5814.

81 J. Yu, Y. Qin, X. Wang, H. Zheng, K. Gao, H. Yang, L. Xie, Q. Hu and C. He, Boosting electrochemical nitrate-ammonia conversion via organic ligands-tuned proton transfer, *Nano Energy*, 2022, **103**, 107705.

82 X. Deng, Y. Yang, L. Wang, X. Z. Fu and J. L. Luo, Metallic Co nanoarray catalyzes selective $NH_3$ production from electrochemical nitrate reduction at current densities exceeding 2 A $cm^{-2}$, *Adv. Sci.*, 2021, **8**, 2004523.

83 J. Wang, J. Liang, P. Liu, Z. Yan, L. Cui, L. Yue, L. Zhang, Y. Ren, T. Li, Y. Luo, Q. Liu, X. E. Zhao, N. Li, B. Tang, Y. Liu, S. Gao, A. M. Asiri, H. Hao, R. Gao and X. Sun, Biomass Juncus derived carbon decorated with cobalt nanoparticles enables high-efficiency ammonia electrosynthesis by nitrite reduction, *J. Mater. Chem. A*, 2022, **10**, 2842–2848.

84 N. Zhang, J. Shang, X. Deng, L. Cai, R. Long, Y. Xiong and Y. Chai, Governing interlayer strain in bismuth nanocrystals for efficient ammonia electrosynthesis from nitrate reduction, *ACS Nano*, 2022, **16**, 4795–4804.

85 Q. Chen, J. Liang, Q. Liu, K. Dong, L. Yue, P. Wei, Y. Luo, Q. Liu, N. Li, B. Tang, A. A. Alshehri, M. S. Hamdy, Z. Jiang and X. Sun, Co nanoparticle-decorated pomelo-peel-derived carbon enabled high-efficiency electro-

Published on 02 May 2023. Downloaded on 2/6/2026 6:54:49 PM.

catalytic nitrate reduction to ammonia, *Chem. Commun.*, 2022, **58**, 4259–4262.

86 K. Wang, R. Mao, R. Liu, J. Zhang and X. Zhao, Sulfur-dopant-promoted electrocatalytic reduction of nitrate by a self-supported iron cathode: selectivity, stability, and underlying mechanism, *Appl. Catal., B*, 2022, **319**, 121862.

87 C. Wang, W. Zhou, Z. Sun, Y. Wang, B. Zhang and Y. Yu, Integrated selective nitrite reduction to ammonia with tetrahydroisoquinoline semi-dehydrogenation over a vacancy-rich Ni bifunctional electrode, *J. Mater. Chem. A*, 2021, **9**, 239.

88 J. Chen, Q. Zhou, L. Yue, D. Zhao, L. Zhang, Y. Luo, Q. Liu, N. Li, A. A. Alshehri, M. S. Hamdy, F. Gong and X. Sun, Co–NCNT nanohybrid as a highly active catalyst for the electroreduction of nitrate to ammonia, *Chem. Commun.*, 2022, **58**, 3787–3790.

89 T. Xie, X. Li, J. Li, J. Chen, S. Sun, Y. Luo, Q. Liu, D. Zhao, C. Xu, L. Xie and X. Sun, Co nanoparticles decorated corncob-derived biomass carbon as an efficientelectrocatalyst for nitrate reduction to ammonia, *Inorg. Chem.*, 2022, **61**, 14195–14200.

90 Z. Fang, Z. Jin, S. Tang, P. Li, P. Wu and G. Yu, Porous two-dimensional iron-cyano nanosheets for high-rate electrochemical nitrate reduction, *ACS Nano*, 2022, **16**, 1072–1081.

91 A. Iarchuk, A. Dutta and P. Broekmann, Novel Ni foam catalysts for sustainable nitrate to ammonia electroreduction, *J. Hazard. Mater.*, 2022, **439**, 129504.

92 P. Gao, Z. H. Xue, S. N. Zhang, D. Xu, G. Y. Zhai, Q. Y. Li, J. S. Chen and X. H. Li, Schottky barrier-induced surface electric field boosts universal reduction of $NO_x^-$ in water to ammonia, *Angew. Chem., Int. Ed.*, 2021, **60**, 20711–20716.

93 Z. Tang, Z. Bai, X. Li, L. Ding, B. Zhang and X. Chang, Chloride-derived bimetallic Cu-Fe nanoparticles for high-selective nitrate-to-ammonia electrochemical catalysis, *Processes*, 2022, **10**, 751.

94 Y. Wang, A. Xu, Z. Wang, L. Huang, J. Li, F. Li, J. Wicks, M. Luo, D. H. Nam, C. S. Tan, Y. Ding, J. Wu, Y. Lum, C. T. Dinh, D. Sinton, G. Zheng and E. H. Sargent, Enhanced nitrate-to-ammonia activity on copper-nickel alloys via tuning of intermediate adsorption, *J. Am. Chem. Soc.*, 2020, **142**, 5702–5708.

95 Y. Liu, B. Deng, K. Li, H. Wang, Y. Sun and F. Dong, Metal-organic framework derived carbon-supported bimetallic copper-nickel alloy electrocatalysts for highly selective nitrate reduction to ammonia, *J. Colloid Interface Sci.*, 2022, **614**, 405–414.

96 T. H. Jeon, Z. Y. Wu, F. Y. Chen, W. Choi, P. J. J. Alvarez and H. Wang, Cobalt-copper nanoparticles on three-dimensional substrate for efficient ammonia synthesis via electrocatalytic nitrate reduction, *J. Phys. Chem. C*, 2022, **126**, 6982–6989.

97 J. Yuan, Z. Xing, Y. Tang and C. Liu, Tuning the oxidation state of Cu Electrodes for selective electrosynthesis of ammonia from nitrate, *ACS Appl. Mater. Interfaces*, 2021, **13**, 52469–52478.

98 T. Ren, K. Ren, M. Wang, M. Liu, Z. Wang, H. Wang, X. Li, L. Wang and Y. Xu, Concave-convex surface oxide layers over copper nanowires boost electrochemical nitrate-to-ammonia conversion, *Chem. Eng. J.*, 2021, **426**, 130759.

99 Q. Hu, Y. Qin, X. Wang, Z. Wang, X. Huang, H. Zheng, K. Gao, H. Yang, P. Zhang, M. Shao and C. He, Reaction intermediate-mediated electrocatalyst synthesis favors specified facet and defect exposure for efficient nitrate–ammonia conversion, *Energy Environ. Sci.*, 2021, **14**, 4989–4997.

100 Z. Gong, W. Zhong, Z. He, Q. Liu, H. Chen, D. Zhou, N. Zhang, X. Kang and Y. Chen, Regulating surface oxygen species on copper(I) oxides via plasma treatment for effective reduction of nitrate to ammonia, *Appl. Catal., B*, 2022, **305**, 121021.

101 J. Geng, S. Ji, H. Xu, C. Zhao, S. Zhang and H. Zhang, Electrochemical reduction of nitrate to ammonia in a fluidized electrocatalysis system with oxygen vacancy-rich $CuO_x$ nanoparticles, *Inorg. Chem. Front.*, 2021, **8**, 5209–5213.

102 H. Wang, Y. Guo, C. Li, H. Yu, K. Deng, Z. Wang, X. Li, Y. Xu and L. Wang, $Cu/CuO_x$ in-plane heterostructured nanosheetarrays with rich oxygen vacancies enhance nitrate electroreduction to ammonia, *ACS Appl. Mater. Interfaces*, 2022, **14**, 34761–34769.

103 S. Liu, L. Cui, S. Yin, H. Ren, Z. Wang, Y. Xu, X. Li, L. Wang and H. Wang, Heterointerface-triggered electronic structure reformation: Pd/CuO nano-olives motivate nitrite electroreduction to ammonia, *Appl. Catal., B*, 2022, **319**, 121876.

104 Y. Xu, Y. Sheng, M. Wang, T. Ren, K. Shi, Z. Wang, X. Li, L. Wang and H. Wang, Interface coupling induced built-in electric fields boost electrochemical nitrate reduction to ammonia over $CuO@MnO_2$ core-shell hierarchical nanoarrays, *J. Mater. Chem. A*, 2022, **10**, 16883–16890.

105 W. Qiu, X. Chen, Y. Liu, D. Xiao, P. Wang, R. Li, K. Liu, Z. Jin and P. Li, Confining intermediates within a catalytic nanoreactor facilitates nitrate-to-ammonia electrosynthesis, *Appl. Catal., B*, 2022, **315**, 121548.

106 Y. Wang, W. Zhou, R. Jia, Y. Yu and B. Zhang, Unveiling the activity origin of a copper-based electrocatalyst for selective nitrate reduction to ammonia, *Angew. Chem., Int. Ed.*, 2020, **59**, 5350–5354.

107 Y. Guo, R. Zhang, S. Zhang, Y. Zhao, Q. Yang, Z. Huang, B. Dong and C. Zhi, Pd doping-weakened intermediate adsorption to promote electrocatalytic nitrate reduction on $TiO_2$ nanoarrays for ammonia production and energy supply with zinc-nitrate batteries, *Energy Environ. Sci.*, 2021, **14**, 3938–3944.

108 J. Gao, B. Jiang, C. Ni, Y. Qi, Y. Zhang, N. Oturan and M. A. Oturan, Non-precious $Co_3O_4$-$TiO_2$/Ti cathode based electrocatalytic nitrate reduction: preparation, performance and mechanism, *Appl. Catal., B*, 2019, **254**, 391–402.

This journal is © the Partner Organisations 2023

Published on 02 May 2023. Downloaded on 2/6/2026 6:54:49 PM.

109 R. Jia, Y. Wang, C. Wang, Y. Ling, Y. Yu and B. Zhang, Boosting selective nitrate electroreduction to ammonium by constructing oxygen vacancies in $TiO_2$, *ACS Catal.*, 2020, **10**, 3533–3540.

110 Z. Wei, X. Niu, H. Yin, S. Yu and J. Li, Synergistic effect of oxygen defects and hetero-phase junctions of $TiO_2$ for selective nitrate electroreduction to ammonia, *Appl. Catal., A*, 2022, **636**, 118596.

111 D. Zhao, C. Ma, J. Li, R. Li, X. Fan, L. Zhang, K. Dong, Y. Luo, D. Zheng, S. Sun, Q. Liu, Q. Li, Q. Lu and X. Sun, Direct eight-electron $NO_3^-$-to-$NH_3$ conversion: using a Co-doped $TiO_2$ nanoribbon array as a high-efficiency electrocatalyst, *Inorg. Chem. Front.*, 2022, **9**, 6412–6417.

112 X. Fan, D. Zhao, Z. Deng, L. Zhang, J. Li, Z. Li, S. Sun, Y. Luo, D. Zheng, Y. Wang, B. Ying, J. Zhang, A. Alshehri, Y. Lin, C. Tang, X. Sun and Y. Zheng, Constructing Co@$TiO_2$ nanoarray heterostructure with schottky contact for selective electrocatalytic nitrate reduction to ammonia, *Small*, 2023, **19**, 2208036.

113 X. He, J. Li, R. Li, D. Zhao, L. Zhang, X. Ji, X. Fan, J. Chen, Y. Wang, Y. Luo, D. Zheng, L. Xie, S. Sun, Z. Cai, Q. Liu, K. Ma and X. Sun, Ambient ammonia synthesis via nitrate electroreduction in neutral media on $Fe_3O_4$ nanoparticles-decorated $TiO_2$ nanoribbon array, *Inorg. Chem.*, 2023, **62**, 25–29.

114 H. Wang, D. Zhao, C. Liu, X. Fan, Z. Li, Y. Luo, D. Zheng, S. Sun, J. Chen, J. Zhang, Y. Liu, S. Gao, F. Gong and X. Sun, $FeS_2$@$TiO_2$ nanobelt array enabled high-efficiency electrocatalytic nitrate reduction to ammonia, *J. Mater. Chem. A*, 2022, **10**, 24462–24467.

115 Z. Deng, C. Ma, X. Fan, Z. Li, Y. Luo, S. Sun, D. Zheng, Q. Liu, J. Du, Q. Lu, B. Zheng and X. Sun, Construction of CoP/$TiO_2$ nanoarray for enhanced electrochemical nitrate reduction to ammonia, *Mater. Today Phys.*, 2022, **28**, 100854.

116 X. Fan, L. Xie, J. Liang, Y. Ren, L. Zhang, L. Yue, T. Li, Y. Luo, N. Li, B. Tang, Y. Liu, S. Gao, A. A. Alshehri, Q. Liu, Q. Kong and X. Sun, In situ grown $Fe_3O_4$ particle on stainless steel: A highly efficient electrocatalyst for nitrate reduction to ammonia, *Nano Res.*, 2022, **15**, 3050–3055.

117 Z. Niu, S. Fan, X. Li, Z. Liu, J. Wang, J. Duan, M. O. Tade and S. Liu, Facile tailoring of the electronic structure and the d-band center of copper-doped cobaltate for efficient nitrate electrochemical hydrogenation, *ACS Appl. Mater. Interfaces*, 2022, **14**, 35477–35484.

118 Z. Deng, C. Ma, Z. Li, Y. Luo, L. Zhang, S. Sun, Q. Liu, J. Du, Q. Lu, B. Zheng and X. Sun, High-efficiency electrochemical nitrate reduction to ammonia on a $Co_3O_4$ nanoarray catalyst with cobalt vacancies, *ACS Appl. Mater. Interfaces*, 2022, **14**, 46595–46602.

119 P. Wei, J. Liang, Q. Liu, L. Xie, X. Tong, Y. Ren, T. Li, Y. Luo, N. Li, B. Tang, A. M. Asiri, M. S. Hamdy, Q. Kong, Z. Wang and X. Sun, Iron-doped cobalt oxide nanoarray for efficient electrocatalytic nitrate-to-ammonia conversion, *J. Colloid Interface Sci.*, 2022, **615**, 636–642.

120 J. Li, D. Zhao, L. Zhang, L. Yue, Y. Luo, Q. Liu, N. Li, A. A. Alshehri, M. S. Hamdy, Q. Li and X. Sun, A $FeCo_2O_4$ nanowire array enabled electrochemical nitrate conversion to ammonia, *Chem. Commun.*, 2022, **58**, 4480–4483.

121 Q. Liu, L. Xie, J. Liang, Y. Ren, Y. Wang, L. Zhang, L. Yue, T. Li, Y. Luo, N. Li, B. Tang, Y. Liu, S. Gao, A. A. Alshehri, I. Shakir, P. O. Agboola, Q. Kong, Q. Wang, D. Ma and X. Sun, Ambient ammonia synthesis via electrochemical-reduction of nitrate enabled by $NiCo_2O_4$ nanowire array, *Small*, 2022, **18**, 2106961.

122 Z. Li, J. Liang, Q. Liu, L. Xie, L. Zhang, Y. Ren, L. Yue, N. Li, B. Tang, A. A. Alshehri, M. S. Hamdy, Y. Luo, Q. Kong and X. Sun, High-efficiency ammonia electrosynthesis via selective reduction of nitrate on $ZnCo_2O_4$ nanosheet array, *Mater. Today Phys.*, 2022, **23**, 100619.

123 L. Xie, L. Hu, Q. Liu, S. Sun, L. Zhang, D. Zhao, Q. Liu, J. Chen, J. Li, L. Ouyang, A. Alshehri, Q. Kong and X. Sun, High-performance electrochemical nitrate reduction to ammonia under ambient conditions using $NiFe_2O_4$ nanosheet arrays, *Inorg. Chem. Front.*, 2022, **9**, 3392–3397.

124 X. Lu, J. Yu, J. Cai, Q. Zhang, S. Yang, L. Gu, G. I. N. Waterhouse, S. Q. Zang, B. Yang and S. Lu, Exclusive nitrate to ammonia conversion via boron-doped carbon dots induced surface Lewis acid sites, *Cell Rep. Phys. Sci.*, 2022, **3**, 100961.

125 H. Liu, J. Li, F. Du, L. Yang, S. Huang, J. Gao, C. Li and C. Guo, A core-shell copper oxides-cobalt oxides heterostructure nanowire arrays for nitrate reduction to ammonia with high yield rate, *Green Energy Environ.*, 2022, DOI: 10.1016/j.gee.2022.03.003.

126 W. Fu, Z. Hu, Y. Du, P. Su, Y. Su, Q. Zhang and M. Zhou, Building dual active sites $Co_3O_4$/Cu electrode to break scaling relations for enhancement of electrochemical reduction of nitrate to high-value ammonia, *J. Hazard. Mater.*, 2022, **434**, 128887.

127 X. Fan, C. Ma, D. Zhao, Z. Deng, L. Zhang, Y. Wang, Y. Luo, D. Zheng, T. Li, J. Zhang, S. Sun, Q. Lu and X. Sun, Unveiling selective nitrate reduction to ammonia with $Co_3O_4$ nanosheets/$TiO_2$ nanobelt heterostructure catalyst, *J. Colloid Interface Sci.*, 2023, **630**, 714–720.

128 M. Chen, J. Bi, X. Huang, T. Wang, Z. Wang and H. Hao, $Bi_2O_3$ nanosheets arrays in-situ decorated on carbon cloth for efficient electrochemical reduction of nitrate, *Chemosphere*, 2021, **278**, 130386.

129 H. Wang, Q. Mao, T. Ren, T. Zhou, K. Deng, Z. Wang, X. Li, Y. Xu and L. Wang, Synergism of interfaces and defects: Cu/oxygen vacancy-rich Cu-$Mn_3O_4$ heterostructured ultrathin nanosheet arrays for selective nitrate electroreduction to ammonia, *ACS Appl. Mater. Interfaces*, 2021, **13**, 44733–44741.

130 J. Wang, D. Wu, M. Li, X. Wei, X. Yang, M. Shao and M. Gu, Bismuth ferrite as an electrocatalyst for the electrochemical nitrate reduction, *Nano Lett.*, 2022, **22**, 5600–5606.

131 Z. Gong, W. Zhong, Z. He, C. Jia, D. Zhou, N. Zhang, X. Kang and Y. Chen, Improving electrochemical nitrate

Published on 02 May 2023. Downloaded on 2/6/2026 6:54:49 PM.

reduction activity of layered perovskite oxide $La_2CuO_4$ via B-site doping, *Catal. Today*, 2022, **402**, 259–265.

132 F. Du, J. Li, C. Wang, J. Yao, Z. Tan, Z. Yao, C. Li and C. Guo, Active sites-rich layered double hydroxide for nitrate-to-ammonia production with high selectivity and stability, *Chem. Eng. J.*, 2022, **434**, 134641.

133 X. Wan, W. Guo, X. Dong, H. Wu, X. Sun, M. Chu, S. Han, J. Zhai, W. Xia, S. Jia, M. He and B. Han, Boosting nitrate electroreduction to ammonia on $NbO_x$ via constructing oxygen vacancies, *Green Chem.*, 2022, **24**, 1090–1095.

134 J. Wang, C. Cai, Y. Wang, X. Yang, D. Wu, Y. Zhu, M. Li, M. Gu and M. Shao, Electrocatalytic reduction of nitrate to ammonia on low-cost ultrathin $CoO_x$ nanosheets, *ACS Catal.*, 2021, **11**, 15135–15140.

135 S. Zhang, M. Li, J. Li, Q. Song and X. Liu, High-ammonia selective metal-organic framework–derived Co-doped Fe/$Fe_2O_3$ catalysts for electrochemical nitrate reduction, *Proc. Natl. Acad. Sci. U. S. A.*, 2022, **119**, e2115504119.

136 X. Fan, J. Liang, L. Zhang, D. Zhao, L. Yue, Y. Luo, Q. Liu, L. Xie, N. Li, B. Tang, Q. Kong and X. Sun, Enhanced electrocatalytic nitrate reduction to ammonia using plasma-induced oxygen vacancies in $CoTiO_{3-x}$ nanofiber, *Carbon Neutralization*, 2022, **1**, 6–13.

137 D. Chen, S. Zhang, X. Bu, R. Zhang, Q. Quan, Z. Lai, W. Wang, Y. Meng, D. Yin, S. Yip, C. Liu, C. Zhi and J. C. Ho, Synergistic modulation of local environment for electrochemical nitrate reduction via asymmetric vacancies and adjacent ion clusters, *Nano Energy*, 2022, **98**, 107338.

138 Q. L. Hong, J. Zhou, Q. G. Zhai, Y. C. Jiang, M. C. Hu, X. Xiao, S. N. Li and Y. Chen, Cobalt phosphide nanorings towards efficient electrocatalytic nitrate reduction to ammonia, *Chem. Commun.*, 2021, **57**, 11621–11624.

139 Y. Jia, Y. G. Ji, Q. Xue, F. M. Li, G. T. Zhao, P. J. Jin, S. N. Li and Y. Chen, Efficient nitrate-to-ammonia electroreduction at cobalt phosphide nanoshuttles, *ACS Appl. Mater. Interfaces*, 2021, **13**, 45521–45527.

140 Q. Yao, J. Chen, S. Xiao, Y. Zhang and X. Zhou, Selective electrocatalytic reduction of nitrate to ammonia with nickel phosphide, *ACS Appl. Mater. Interfaces*, 2021, **13**, 30458–30467.

141 J. Liang, B. Deng, Q. Liu, G. Wen, Q. Liu, T. Li, Y. Luo, A. A. Alshehri, K. A. Alzahrani, D. Ma and X. Sun, High-efficiency electrochemical nitrite reduction to ammonium using a $Cu_3P$ nanowire array under ambient conditions, *Green Chem.*, 2021, **23**, 5487–5493.

142 G. Wen, J. Liang, Q. Liu, T. Li, X. An, F. Zhang, A. A. Alshehri, K. A. Alzahrani, Y. Luo, Q. Kong and X. Sun, Ambient ammonia production via electrocatalytic nitrite reduction catalyzed by a CoP nanoarray, *Nano Res.*, 2022, **15**, 972–977.

143 S. Ye, Z. Chen, G. Zhang, W. Chen, C. Peng, X. Yang, L. Zheng, Y. Li, X. Ren, H. Cao, D. Xue, J. Qiu, Q. Zhang and J. Liu, Elucidating the activity, mechanism and application of selective electrosynthesis of ammonia from nitrate on cobalt phosphide, *Energy Environ. Sci.*, 2022, **15**, 760–770.

144 Q. Yao, J. Chen, S. Xiao, Y. Zhang and X. Zhou, Selective electrocatalytic reduction of nitrate to ammonia with nickel phosphide, *ACS Appl. Mater. Interfaces*, 2021, **13**, 30458–30467.

145 F. Ni, Y. Ma, J. Chen, W. Luo and J. Yang, Boron-iron nanochains for selective electrocatalytic reduction of nitrate, *Chin. Chem. Lett.*, 2021, **32**, 2073–2078.

146 X. Liu, X. Xu, F. Li, J. Xu, H. Ma, X. Sun, D. Wu, C. Zhang, X. Ren and Q. Wei, Heterostructured $Bi_2S_3$/$MoS_2$ nanoarrays for efficient electrocatalytic nitrate reduction to ammonia under ambient conditions, *ACS Appl. Mater. Interfaces*, 2022, **14**, 38835–38843.

147 Z. Li, G. Wen, J. Liang, T. Li, Y. Luo, Q. Kong, X. Shi, A. M. Asiri, Q. Liu and X. Sun, High-efficiency nitrate electroreduction to ammonia on electrodeposited cobalt–phosphorus alloy film, *Chem. Commun.*, 2021, **57**, 9720.

148 X. Zhang, G. Ma, L. Shui, G. Zhou and X. Wang, $Ni_3N$ nanoparticles on porous nitrogen-doped carbon nanorods for nitrate electroreduction, *Chem. Eng. J.*, 2022, **430**, 132666.

149 Y. Shi, S. Xu and F. Li, Electrocatalytic nitrate reduction to ammonia via amorphous cobalt boride, *Chem. Commun.*, 2022, **58**, 8714–8717.

150 Y. Wang, L. Zhang, Y. Niu, D. Fang, J. Wang, Q. Su and C. Wang, Boosting $NH_3$ production from nitrate electroreduction via electronic structure engineering of $Fe_3C$ nanoflakes, *Green Chem.*, 2021, **23**, 7594–7608.

This journal is © the Partner Organisations 2023